# Microdosed Lipid-Coated $^{67}$Ga-Magnetite Enhances Antigen-Specific Immunity by Image Tracked Delivery of Antigen and CpG to Lymph Nodes

*Ane Ruiz-de-Angulo,[1] Aintzane Zabaleta,[1] Vanessa Gomez Vallejo,[2] Jordi Llop[3] and Juan C. Mareque-Rivas[1,4,]**

[1]Theranostic Nanomedicine Laboratory, Cooperative Centre for Research in Biomaterials (CIC biomaGUNE), Paseo Miramón 182, 20009-San Sebastián, Spain.

[2]Radiochemistry Platform, Cooperative Centre for Research in Biomaterials (CIC biomaGUNE), Paseo Miramón 182, 20009-San Sebastián, Spain

[3]Radiochemistry and Nuclear Imaging, Cooperative Centre for Research in Biomaterials (CIC biomaGUNE), Paseo Miramón 182, 20009-San Sebastián, Spain.

[4]IKERBASQUE, Basque Foundation for Science, 48011-Bilbao, Spain

**Corresponding Author**

* Address correspondence to: jmareque@cicbiomagune.es

**KEYWORDS**: multifunctional nanoparticles, multimodal imaging, synthetic vaccines, Toll-like receptors, drug delivery, immunotherapy, theranostics,

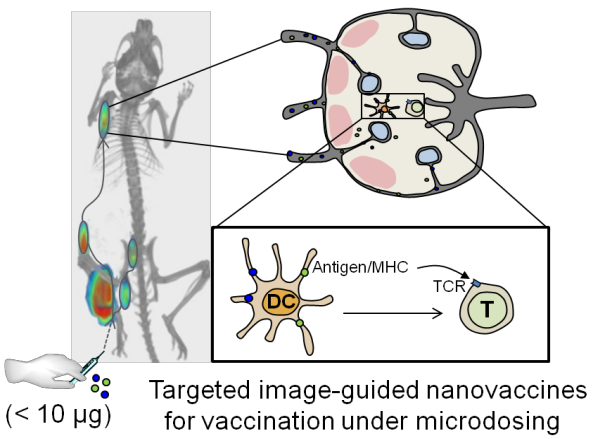


**ABSTRACT**: Development of vaccines to prevent and treat emerging new pathogens and re-emerging infections and cancer remains a major challenge. An attractive but virtually unexplored approach is to build the vaccine upon a biocompatible NP which simultaneously acts as accurate delivery vehicle and radiotracer for PET/SPECT imaging for ultrasensitive and quantitative *in vivo* imaging of NP delivery to target tissues/organs. Success in developing these new nanovaccines will depend in part on having a ´correct´ NP size and accommodating and suitably displaying antigen and/or adjuvants (e.g. TLR agonists). Here we develop and evaluate a new NP vaccine based on iron oxide-selective radio-gallium labeling suitable for SPECT($^{67}$Ga)/PET($^{68}$Ga) imaging and efficient delivery of antigen (OVA) and TLR 9 agonists (CpGs) using lipid-coated magnetite micelles. OVA, CpGs and rhodamine (for *in vitro* tracking) are easily accommodated in the hybrid micelles and the average size of the construct can be controlled to be ca. 40 nm in diameter to target direct lymphatic delivery of the vaccine cargo to antigen presenting cells (APCs) in the lymph nodes (LNs). Whilst the OVA/CpG-loaded construct showed effective delivery to endosomal TLR 9 in APCs, SPECT imaging demonstrated migration from the injection site to regional and non-regional LNs. In correlation with the imaging results, a range of *in vitro* and *in vivo* studies demonstrate that by using this microdosed nanosystem the cellular and humoral immune responses are greatly enhanced. These results suggest that these nanosystems have considerable potential for image-guided development of new targeted vaccines which are more effective and limit toxicity.

## INTRODUCTION

Many pathogens and cancer cells have evolved mechanisms to evade the host immune response, leaving current vaccine strategies inadequate for providing an effective protection against emerging new pathogens and re-emerging infections or fighting cancer.[1] Although subunit vaccines based on protein or peptide antigens are considered attractive because of their low toxicity and cost and widespread availability and applicability,[2] they have limited efficacy because soluble doses of antigens are rapidly cleared and poorly immunogenic. To overcome these limitations, many studies have focused on antigen delivery using monoclonal antibodies attached to proteins[3,4,5] or microparticles[6,7] for *in vivo* targeting of peripheral dendritic cells (DCs) in tissues such as the skin. However, optimal encounter with naive T cells for the presentation of antigens requires that the DCs migrate to draining lymph nodes (LNs) through lymphatic vessels.[8] Moreover, DCs are present in much higher numbers in the LNs than in peripheral tissues. By targeting antigen delivery to the draining LNs using nanoparticle (NP)-based vehicles the potency of the immune responses could be enhanced.[9,10] However, in addition to targeted antigen delivery developing effective subunit vaccines requires co-administration of an appropriate "danger" signal to stimulate the innate immune system.[11] For this purpose, most rationally designed synthetic vaccines make use of molecules which activate Toll like receptors (TLRs) in immune cells. Among these molecules, synthetic unmethylated cytosine–guanosine motifs (CpG oligodeoxynucleotides (ODNs)) mimic molecular signatures of bacteria and viruses and trigger an immunostimulatory cascade including maturation, differentiation and proliferation of multiple host immune cells through TLR 9 binding and activation.[12] The immunostimulatory features of CpG ODNs have made it a promising tool in immunotherapeutic applications. Unlike

many other TLRs, TLR 9 is not found on the surface of cells, but is initially localized in the endoplasmic reticulum and traffics to the endolysosomes, where the processed form of the receptor can bind CpG-containing structures.[13] It is now accepted that it is ultimately localization to the endolysosomal compartment together with some minimal sequence requirements that dictates TLR 9 activation.[14] Consistent with this cell and chemical biology view of TLR 9 signalling, NPs which enter immune cells via the endocytic pathway should also be ideal to potentiate the activity of CpG ODNs. [15,16,17,18,19]

Over the past few years, different types of NPs have emerged as powerful platform technologies for vaccine delivery. [6,10,16,20,21,22,23,] However, it is now widely accepted that to improve the efficiency of the overall drug discovery and development (DDD) process it is also critically important to integrate molecular imaging approaches.[24,25,26] Imaging not only streamlines DDD but also allows new opportunities in treatment management of targeted therapies by improving patient selection, predicting response to therapy and/or toxicity, optimization of the duration, dose and schedule of treatment etc. Thus, together with advances in NP-design, synthesis and biofunctionalisation to precisely target and optimize a specific biological response, there is a growing need for incorporating imaging features in NPs to gain better understanding and predict how they will respond and be processed *in vivo*. So far few studies have investigated the effect of antigen and/or CpG delivery using inorganic NPs to combine high immunostimulatory activity with non invasive *in vivo* imaging. Gold NPs have been investigated for this purpose because they combine many attractive features such as low toxicity and easy and versatile synthesis with the possibility of *in vivo* tracking using X-ray computed tomography.[15,27,17,19] However, *in vivo* CT detection of gold NP biodistribution is limited by the large amount of gold that must be delivered and accumulated at the target site for detecting the NP (1.7 g per CT scan is predicted

to be required for tumor imaging in humans),[28] which is impracticable and restrictive for many applications. Although great progress and results have resulted from using these new NP vaccine delivery systems, effective systems which combine facile synthesis with effective delivery and imaging features under microdosing conditions are needed to facilitate clinical translation of nanovaccines.

The use of biocompatible iron oxide NPs (IONPs) such as magnetite presents the advantage that IONPs are widely considered the most clinically translatable and versatile materials for biomedicine.[29,30,31] Although magnetite NPs can be intrinsically detected by Magnetic Resonance Imaging (MRI) and have been safely used in humans as MRI contrast agents in diagnostic imaging,[32, 33] these experiments also require administration of quite high NP concentrations. Furthermore, ready quantification of the MRI signal for whole-body biodistribution study purposes is not feasible. As a result, relying exclusively on MRI for NP-tracking is not satisfactory or possible for many diagnostic and therapeutic applications.[34]

Compared to MRI and CT, one of the major advantages of single photon emission computed tomography (SPECT) and positron emission tomography (PET) as non-invasive molecular imaging techniques is their high sensitivity, which permits the detection and accurate quantitation of extremely low amounts of the drug-loaded nanocarrier. However, the potential to use these imaging techniques to improve the DDD process, predict *in vivo* behavior and facilitate clinical translation of NP-based systems will depend to a large extent on the successful development of new, simple and effective radiolabelling strategies for NPs. So far most studies have required radiolabeling of inorganic NPs, including IONPs, using organic chemistry-based synthetic procedures.[35,36,37.38,39,40,41,42] In addition to multistep synthesis and low reaction yields, for many applications these approaches rely on identifying and carrying out orthogonal reactions

for co-functionalizing with targeting ligands or therapeutic agents. A further caveat is that high loading of organic chelates on the surface of the NP can alter the pharmacological and/or pharmacokinetic properties of the NP leading to suboptimal targeting and biodistribution. To overcome this limitations a few chelate-free approaches for radiolabeling inorganic NPs have been recently reported.[43,44,45,46]

We report herein a new approach in antigen and CpG delivery and gallium NP radiolabeling which exploits a specific size (ca. 40 nm) and surface properties of magnetite-filled PEGylated phospholipid (PEG-PLs) micelles to promote direct attachment of $Ga^{3+}$ ions and *in vivo* LN targeting. We demonstrate that radiolabeling with $^{67}Ga^{3+}$ is very efficient for IONP-filled micelles even without macrocyclic chelators but not for identical micelles filled with CdSe/ZnS QDs. The IONP filled micelles could be easily coated with a fluorescent dye and the model antigen ovalbumin (OVA) or pathogen mimetic CpG ODNs without affecting the size of the nanoconstruct. By using fluorescence imaging the endocytic uptake of the biofunctional IONP-filled micelles and subsequent cytokine production and maturation in the target cells are investigated and correlated. SPECT imaging allows efficient tracking of the delivery vehicles *in vivo* from which it is possible to correlate migration via the lymphatic system to reach LNs with the immunization results, which show that the nanocarriers enhance the efficacy of the vaccine by maintaining potent antigen-specific humoral and cellular immunity under microdosing conditions.

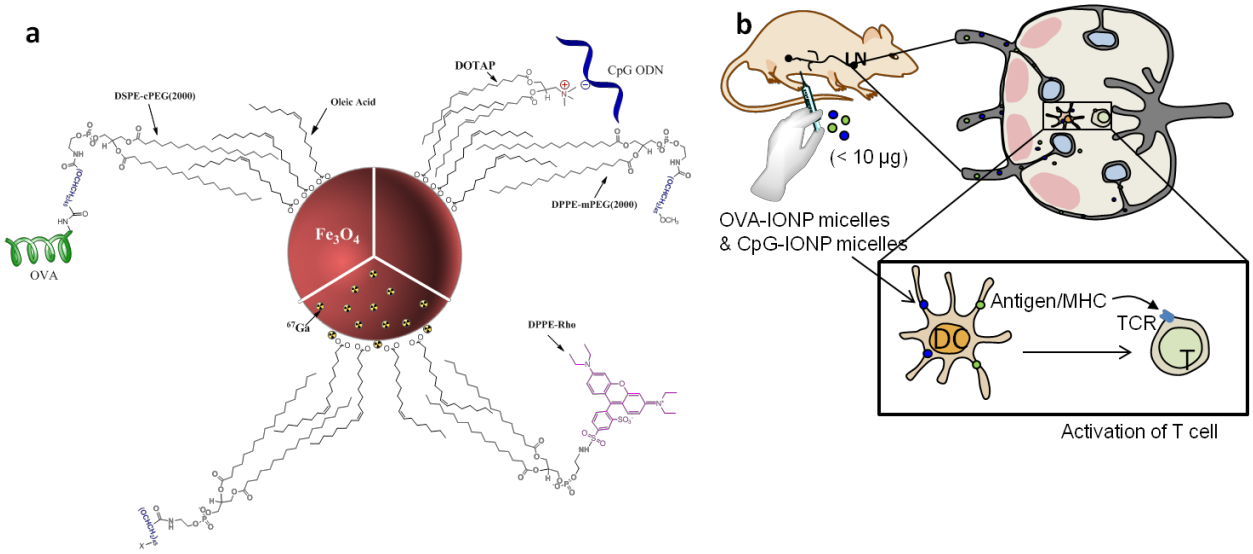


**Scheme 1.** a) Schematic representation of the strategies used for the preparation of OVA-IONP and CpG-IONP micelles and for organic chemistry-free $^{67}$Ga and Rhodamine labeling. b) The microdosed nanosystem with average diameter of ca. 40 nm is designed to provide effective lymphatic delivery of the vaccine components to secondary lymphoid organs such as the lymph nodes where uptake by DCs facilitates the induction of potent humoral and cellular immunity.

## RESULTS AND DISCUSSION

**Synthesis and characterization of the nanoparticles.** The preparation of the hydrophobic IONPs was carried out as described in previous publications.[47,48] The characterization of the as prepared oleic acid coated IONPs by transmission electron microscopy (TEM) showed an average IONP diameter of 6.8 nm (Supporting Information, Figure S1). The water soluble IONP-filled micelles were prepared by a variation of the lipid film hydration method with the as prepared hydrophobic IONPs and commercially available PEG-PLs (1,2-dipalmitoyl-*sn*-glycero-3-phosphoethanolamine-N-[methoxy(polyethylene glycol)-2000 (DPPE-mPEG(2000)) and 1,2-distearoyl-*sn*-glycero-3-phosphoethanolamine-N-[carboxy(polyethylene glycol)-2000] (DSPE-

cPEG(2000)); see experimental section).[49] The combination of different lipids allowed the functionalization of the IONP PEG-PL micelles with antigen and synthetic CpG ODNs adopting for each a different strategy of attachment. IONP micelles formed with the PEG PLs were unable to capture the CpG ODNs. In contrast, when the cationic lipid DOTAP (1,2-dioleoyl-3-trimethylammonium-propane) was incorporated in the mixture of PEG PLs it was possible to bind electrostatically the CpG ODNs to the IONP-filled micelles. The attachment of the model antigen ovalbumin (OVA) to the IONP-filled micelles was performed by EDC/NHS-mediated covalent amide bond formation between the amine groups of the protein and the carboxylic groups of the DSPE-cPEG(2000) molecules decorating the IONP-filled micelles. After an overnight incubation of the corresponding IONP micelles with OVA or CpG ODNs, the unbound molecules were removed by filtration and centrifugation and the final concentration of antigen and adjuvant loaded into the IONP micelles was determined. After the elimination of the unbound CpG ODNs, the UV absorption analysis of the sample showed the characteristic peak of the CpG ODNs at 260 nm (Figure 1a). To quantify the amount of CpG ODNs attached to the IONP micelles the sample was hydrolyzed in 0.2 M NaOH, the UV absorbance ($\lambda_{max}$ = 260 nm) of the hydrolyzed CpG ODNs measured and converted to concentration by comparison to a standard curve. The results discussed below are for micelles with an average value of 10 CpG ODN molecules per each IONP (CpG-IONP micelles). Whilst the zeta potential of the parent DOTAP-containing IONP micelles was positive, the CpG-IONP micelles showed a zeta potential of -16.8, consistent with the presence of the negatively charged CpG ODNs (Figure 1b). The size of the IONP-DOTAP micelles and CpG-IONP micelles was determined by dynamic light scattering (DLS) and TEM (Figure 1b,c and Supporting Information Figure S1). Both techniques showed that the diameter of the CpG-IONP micelles remains stable and in the target 10-80 nm

range for at least two weeks after its formation with a mean diameter of 43.25 ± 8.97 nm. The concentration of bound OVA was determined by the BCA method. Moreover, the UV visible absorbance analysis showed the characteristic peak of the OVA at 280 nm with absorption also at 350 nm (characteristic of protein aggregation) after removing the contribution of the parent IONP micelles (Figure 1d). In this study we used OVA-IONP micelles with an OVA-to-IONP molar ratio of 2:1 (OVA-IONP micelles). The characterization by DLS and TEM of the OVA-IONP micelle showed an average diameter of 32.84 ± 6.90 nm (Figure 1e,f and Supporting Information Figure S1) and zeta-potential of -17, which is consistent with the presence of carboxylate end-terminated PEG PLs and negatively charged OVA proteins (pI 4.63).

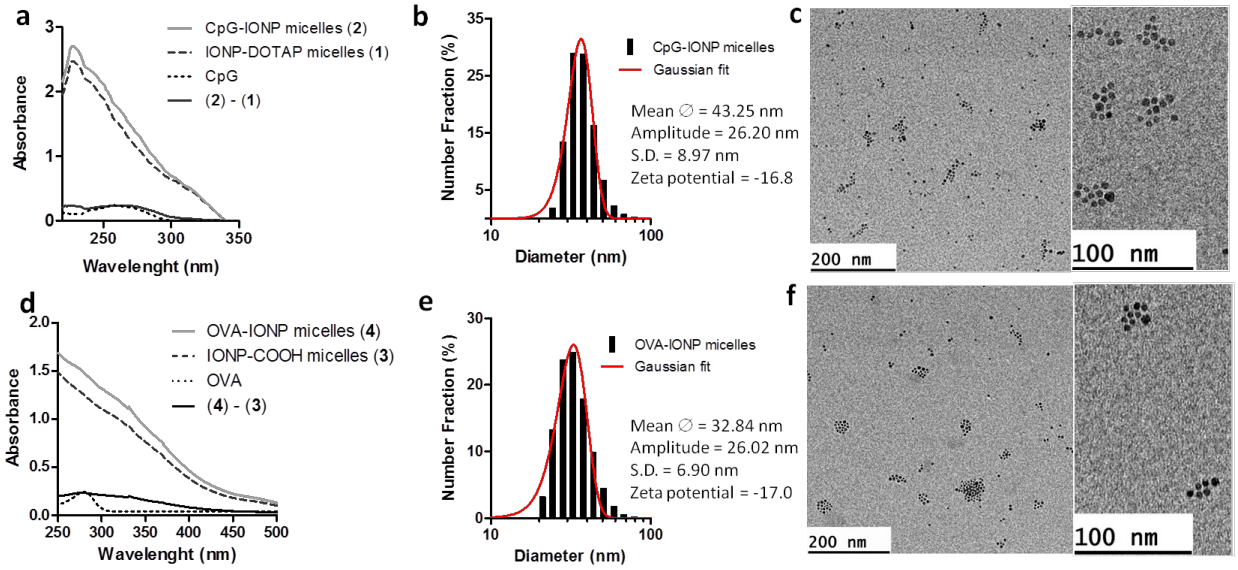


**Figure 1.** Characterization of the CpG-IONP micelles and OVA-IONP micelles. a) UV absorbance spectra of CpG ODNs, IONP-DOTAP micelles, CpG-IONP micelles and CpG-IONP micelles after removing the contribution of the IONP-DOTAP micelle. b) Size distribution obtained by DLS and zeta potential of CpG-IONP micelles. c) Representative TEM images of CpG-IONP micelles. d) UV absorbance spectra of OVA, IONP-COOH micelles, OVA-IONP micelles and OVA-IONP micelles after removing the contribution of the IONP-COOH micelles. e) Size distribution obtained by DLS and zeta potential of the OVA-IONP micelles. f) Representative TEM images of OVA-IONP micelles.

It is now well documented that the size of the nanocarriers is one of the key parameters regulating the *in vivo* biodistribution. Additionally, size can also modulate the biological

responses to the molecules attached to them.[50,51] For targeting lymphatic trafficking and uptake by DCs, 25-40 nm appears to be the optimal size range,[50] and many other *in vivo* applications and drug delivery studies have reported to require 10-100 nm NPs.[52] IONP-filled micellar systems are versatile constructs for developing delivery systems with these size properties (Supporting Information, Figure S2). Here, we show that such micelles are ideal and readily adaptable for creating effective CpG adjuvant and antigen delivery systems by combining simple self-assembly processes with standard conjugation chemistry.

**Organic chelate-free, radio-gallium binding to magnetite-filled PEG-PL micelles.** Currently, PET is considered the most advanced nuclear imaging technique. Among all PET radionuclides, $^{18}$F and $^{68}$Ga are the most widely used in clinical settings. Compared to $^{18}$F ($t_{1/2}$ = 110 minutes), $^{68}$Ga ($t_{1/2}$ = 68 minutes) offers the advantage that it can be obtained from an in-house generator, turning $^{68}$Ga into a more affordable and readily available choice for PET imaging (i.e. its use does not require a nearby cyclotron).[53] Moreover, since $^{67}$Ga is a gamma emitting radionuclide ($t_{1/2}$ = 3.3 days), $Ga^{3+}$ chemistry can also be applied using cheaper and more readily available SPECT systems over longer periods of time. Despite the growing interest in radiolabeling NPs, few inorganic NPs have been successfully radiolabeled with gallium even using organic chelate-based approaches.[54,55,56]

We explored the suitability of direct surface recognition of the radionuclide by the magnetite core. With that aim, the amount of $^{67}$Ga captured by different concentrations of IONP micelles decorated with different PEG-PLs (DPPE-mPEG(2000) and DSPE-cPEG(2000)) was investigated. To ensure the correct interpretation of the radiolabeling results, micelles filled with CdSe/ZnS core/shell QDs with similar nanocrystal core size, surface ligands and PEG-PLs were also prepared as reported elsewhere.[57] For the radio-gallium binding studies, commercially

available $^{67}$Ga citrate was first converted into the more convenient chloride salt. $^{67}$Ga was first trapped in a Sep-Pak® light silica column (Waters), washed with water and finally eluted with HCl 0.1 M solution. The $^{67}$Ga chloride solution (100 μL) was mixed with 50 μL of micelles at the appropriate concentration and diluted up to a final volume of 350 μL in acetate buffer (pH = 3.8). After incubation (70 °C, 30 min), the free $^{67}$Ga was removed by ultrafiltration through an Amicon Ultracel 100k (MWCO 100 kDa) centrifugal device (Merck) at 6708 × g for 10 min (2 cycles); the retentate, containing radiolabeled micelles, was finally resuspended in 10 mM PBS. The magnetite-filled micelles showed excellent $^{67}$Ga capture even at subnanomolar NP concentrations without significant differences arising from the PEG-PLs forming the organic outer surface of the micelle (Figure 2a). This result is consistent with $^{67}$Ga targeting the magnetite core. The current ‘‘gold standard’’ $Ga^{3+}$ chelator in radiolabeling studies is the macrocycle DOTA (1,4,7,10-tetraazacyclododecane-1,4,7,10-tetraacetic acid). Since the QDs exhibited poor $^{67}$Ga binding, we attached DOTA to the CdSe/ZnS QDs by amide bond formation with the PEG-PLs. The $^{67}$Ga capture by the QD-filled micelles functionalized with DOTA was still much lower than for the DOTA-free IONP micelles. Binding to the IONP inorganic nanocrystal appears to be much more favorable than binding to this archetypical $Ga^{3+}$ chelator. Although chemical conjugation of organic chelators to inorganic NPs is the most widely used method for radiolabeling NPs, a few recent studies are beginning to show that resorting to organic chemistry may not be necessary for some inorganic NP.[43,54,45,46] Consistent with our recent results with $^{99m}$Tc labeling of IONPs and QDs,[48,53] the surface of inorganic NPs appears to be a very useful site for binding the radionuclides in a surface-specific manner. In the case of $Ga^{3+}$ binding, a recent study shows that to achieve a high radiolabeling yield even the best chelators have to be used in micromolar concentrations.[59] Thus, a high loading of DOTA would

be required to see its effect in the overall $^{67}$Ga capture capacity of the inorganic NP. Such high loading of DOTA is difficult to achieve in some cases. Even if achieved, the presence of DOTA on the NP surface may affect other properties of the NP. In these inorganic NP-filled micelles the NP:PEG-PL ratio is ca. 1:100.[60] Thus at low NP concentrations even in the case of using exclusively the DOTA-modified PEG-PLs to form the QD-filled micelles it is not possible to reach sufficiently high chelator concentrations to match the strong binding promoted by the magnetite core. We confirmed that the addition of the antigen protein did not interfere in the radiolabeling and that they are stable. Radiolabeled IONPs showed an excellent radiochemical integrity. Even when they were incubated for 24 h in the presence of a large excess of DOTA as competing ligand ($10^6$ moles of DOTA per mol of IONP), >80 % of the radioactivity remained attached to the IONPs (Figure 2b), confirming the formation of strong $Ga^{3+}$-IONP interactions. Taken together these results show that organic chemistry-free radiolabelling with $^{67}Ga^{3+}$ is efficient and specific for the IONP micelles even without macrocyclic chelators. Gallium has been extensively used in biological studies as a redox-inactive iron substitute due to the similarity of $Ga^{3+}$ and $Fe^{3+}$ in charge, size ($Fe^{3+}$ 0.65 Å; $Ga^{3+}$ 0.62 Å)[61] and binding properties.[62,63] Since many biological systems cannot distinguish between these two hard Lewis acids,[64] our results demonstrate that it is feasible exploiting this similarity to induce direct binding of $^{67}Ga^{3+}$ (or $^{68}Ga^{3+}$) to the magnetite core, avoiding the need of previously incorporating an organic metal chelator. In this way, the reactive groups present in the PEG-PLs can be used to covalently attach an antigen and/or adjuvants, and use size-selected IONP as a novel delivery vehicle to promote that the two payloads are targeted to the same cells at the target tissue to improve the vaccine efficacy for inducing potent humoral and cellular immunity at low doses.

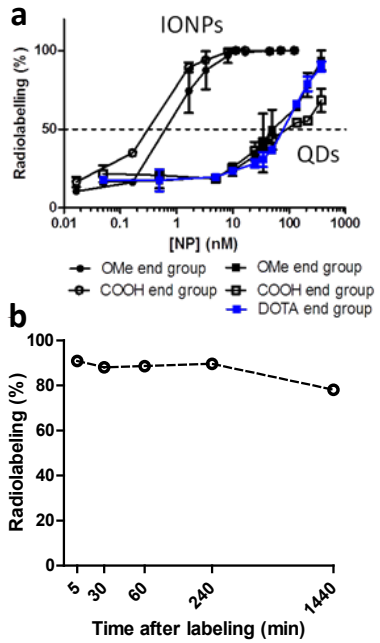


**Figure 2.** a) $^{67}$Ga incorporation efficiency at different NP concentrations for CdSe/ZnS QD- and IONP-filled micelles with OMe, COOH and DOTA end groups (pH 3.8 ± 0.1, 30 min, 70 °C). b) Stability of the radiolabeled IONP micelles. $^{67}$Ga labeled IONP-filled micelles were incubated with $10^6$-fold molar excess of the macrocyclic chelator DOTA.

***In vitro* and *in vivo* trafficking of the CpG- and OVA-functionalized IONP micelles.** The TLR 9 expression in J774 macrophages and bone marrow derived dendritic cells (BMDC) was analyzed with flow cytometry (Supporting Information, Figure S3). Then, the internalization of the CpG- and OVA-functionalized IONP micelles in both types of APCs was investigated by fluorescence microscopy and flow cytometry. For this purpose, these IONP micelles are convenient constructs because they can be fluorescently labeled simply by addition of a commercially available rhodamine B-modified DPPE phospholipid (**DPPE-Rho**) during the solubilization of the hydrophobic IONP by micelle formation. When the percentage of DPPE-Rho is < 5 % it is possible to obtain fluorescent IONP micelles without affecting the size and the attachment of CpG ODNs and OVA (see Supporting Information, Figure S4). The resulting rhodamine-labeled CpG- or OVA-functionalized IONP micelles were incubated with murine

J774A.1 macrophages and bone marrow derived cells (BMDCs) for 3 h. The cellular uptake of the CpG delivery system analyzed by flow cytometry showed efficient micelle uptake by both cell types (Figure 3a, c). To gain further information about the intracellular delivery capacity to the target endosomal TLR 9, the rhodamine-labeled CpG-IONP micelles were analyzed by fluorescence microscopy. The results confirmed the good uptake seen by flow cytometry and showed that the CpG-IONP micelles co-localized with late endosomes/lysosomes, stained with LysoTracker Green. By labeling the TLR 9 with a fluorescent antibody specific for TLR 9, it was possible to confirm that the CpG-IONP micelles are capable of delivering the CpG ODN cargo to TLR 9 in both J774A.1 macrophages and BMDCs (Figure 3b, d).

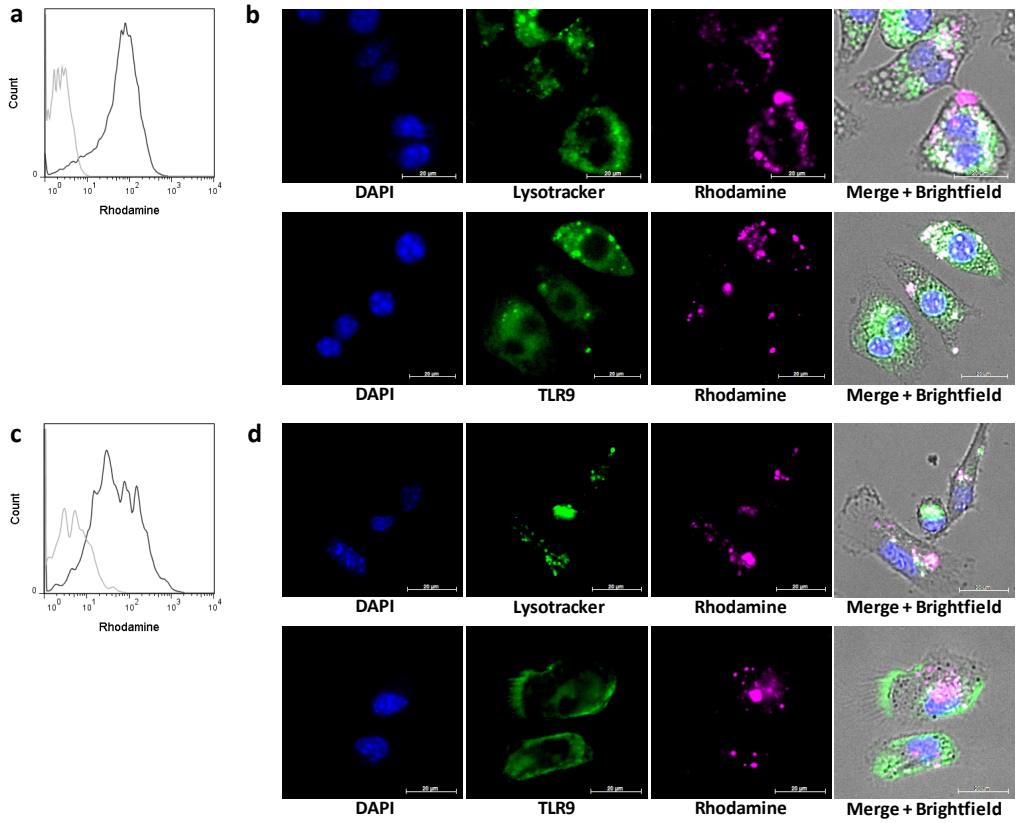


**Figure 3.** Uptake and trafficking of the fluorescently labeled CpG-IONP micelles in (a, b) J774A.1 macrophages and (c, d) BMDCs, after 3 h of incubation with the nanoparticles. Flow cytometry (a, c) and fluorescence microscopy (b, d) shows the cellular uptake and co-localization with endosomes/ lysosomes or TLR 9. Nuclei were stained with DAPI (blue), endosomes and lysosomes were visualized with LysoTracker (green) and TLR 9 was immunolabeled with anti-

TLR 9 antibody combined with Alexa488 (green) secondary antibody. CpG-IONP micelles were labeled with N-lissamine rhodamine dipalmitoylphosphatidylethanolamine (red).

Since antigens entering the endocytic pathway of APCs is critical for the generation of effective adaptive immune responses (MHC class II molecules acquire their peptides in endosomes), the intracellular location of the rhodamine labeled OVA-IONP micelles was investigated in the same way (Figure 4a, c). Flow cytometry shows that the OVA-IONP micelles are taken up by macrophages and BMDCs. The co-localization with endosomes and lysosomes by fluorescent microscopy confirmed the endocytic delivery of OVA in both APCs types (Figure 4b, d).

These fluorescence imaging studies are consistent with other studies which have shown that nanoparticles of 30-60 nm in diameter are well-internalized into cells via the endocytotic pathway.

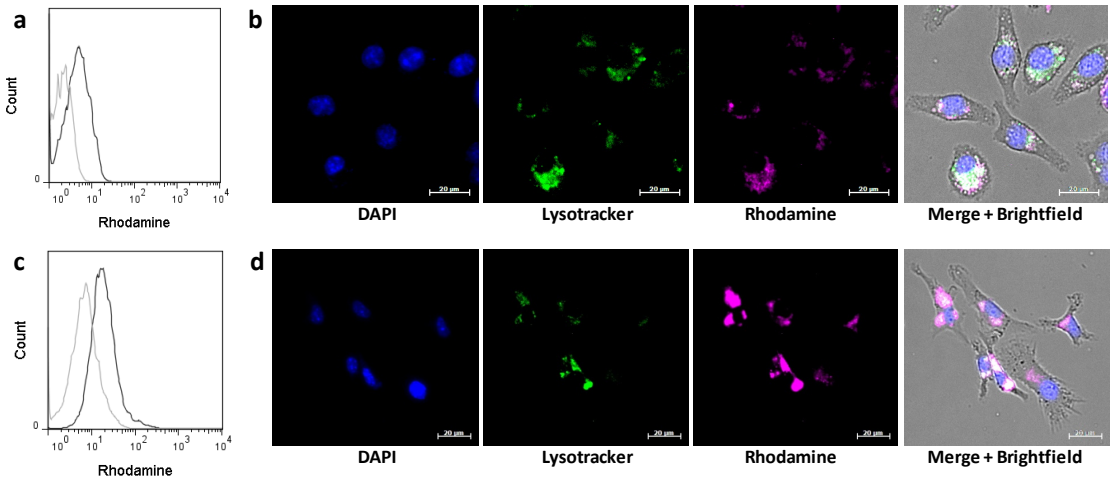


**Figure 4.** Uptake and trafficking of the fluorescently labeled OVA-IONP micelles in (a, b) J774A.1 macrophages and (c, d) mouse bone marrow derived cells, after 3 h of incubation with the nanoparticles. Flow cytometry (a, c) and fluorescence microscopy (b, d) shows the cellular uptake and co-localization with endosomes/ lysosomes. Nuclei were stained with DAPI (blue), endosomes and lysosomes were visualized with LysoTracker (green) and OVA-IONP micelles were labeled with N-lissamine rhodamine dipalmitoylphosphatidylethanolamine (red).

In addition to demonstrating effective *in vitro* delivery to target receptors, identifying the best route of administration is important in the DDD process. Nuclear imaging techniques can provide a rapid and effective way to study the biodistribution and pharmacokinetics while minimising the number of experimental animals in a cost-effective manner. An important current target in cancer therapy and immunotherapy is efficient delivery of drugs and immunotherapeutics through the lymphatic system[9,65,66] to target the draining LNs as key immunological command centres. To investigate the possibility of site-dependent migration to draining LNs after subcutaneous (s.c.) injection of the NP vaccine and how this might affect or be used to predict/explain the *in vivo* efficacy of the system in immunization studies, we tracked the IONP micelles without and with CpG ODN/OVA 3 h and 24 h after s.c. injection in the left flank, forearms and hock of mice using SPECT/CT. The lymphatic drainage pattern was virtually identical for all the IONP micelles, which is consistent with the notion that size is the principle determinant of nanoparticle lymphatic trafficking. SPECT/CT studies showed that 3 h after s.c. injection in the forearm, the IONP micelles already reach the draining left axillary LNs (**Figure 5a** and Supporting Information Figure S5). After s.c. injection in the left hind hock, IONP micelles had migrated to the left inguinal and popliteal LNs at t = 3 h. A clear signal was also detected in the axillary and iliac LNs (Figure 5b and Supporting Information Figure S5), which are directly connected via lymphatic vessels with the inguinal LNs and popliteal LNs respectively.[67] When the s.c. injection was performed in the flank, the intense signal at the site of injection prevented the detection of the IONP micelles in the draining inguinal LNs (Figure 5c). However, *ex vivo* analysis 24 h after inoculation in the flank (Figure 5d-f) shows accumulation of the IONP micelles in the left inguinal LN, as well as in the axillary LN with which it is anatomically connected.[68]

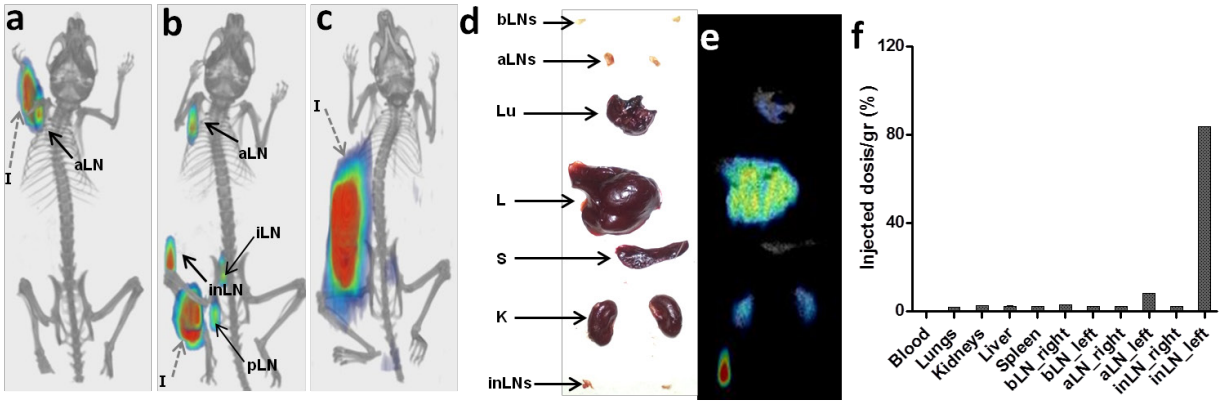


**Figure 5.** SPECT/CT images of mice injected with the $^{67}$Ga labeled IONP micelles 3 h post injection in the left: a) forearm (7.7 MBq), b) hind hock (7.3 MBq) and c) flank (6.4 MBq). *Ex vivo* analysis of the biodistribution after 24 h (s.c. injection in the flank): d) photograph of selected harvested organs, e) SPECT/CT image of the harvested organs and f) biodistribution expressed as percent injected dose per gram of tissue. aLN, axillary LN; inLN, inguinal LN; iLN, iliac LN; pLN, popliteal LN; bLN, braquial LN; Lu, lungs; L, Liver; S, spleen; K, kidneys; injection site (I).

Overall, the fluorescence and SPECT/CT imaging studies show that the IONPs are well-internalized by APCs via the endocytotic pathway and reach the LNs draining the site of injection as well as more distal LNs from different anatomical regions of injection. Therefore through multimodal imaging we could confirm the ability of these size-selected IONP micelles to provide effective endosomal receptor targeting and excellent lymphatic trafficking of vaccine components to the LNs, as one of the recently postulated requirements for inducing potent cellular and humoral immune responses.[16, 13]

***In vitro* and *in vivo* immunostimulatory activity of the CpG- and OVA-functionalized IONP micelles.** The ability of IONP-filled micelles decorated with CpG ODNs to activate cells of the immune system was investigated in the J774A.1 macrophages and BMDCs. After 24 h supernatants were harvested and selected pro-inflammatory cytokines secreted by these cells upon CpG ODN stimulation were quantified by ELISA. The CpG-IONP micelles produced dose-dependent activation of these cells. It was clearly noticeable that IL-6 and TNF-α production in

J774A.1 macrophages treated with the CpG-IONP micelles was much higher than in cells treated with free CpG without nanoparticle-induced cytotoxic effects (Figure 6a, b and Supporting Information, Figure S6 and S7**)**. Similarly, CpG-IONP micelles provide significantly enhanced production of IL-6 and TNF-α in BMDCs without any noticeable cytotoxicity due to the IONP micelle delivery vehicle (Figure 6c-e and Supporting Information, Figure S6 and S7).

In the specific case of DCs apart from cytokine production several other features, including their maturation status and migratory potential, have been shown to be important for induction of effective immune responses against bacteria, viruses and malignant cells.[69,70] The maturation status of BMDCs, as assessed by increased surface expression of CD80 and CD86, was determined by flow cytometry. We observed some increased expression of CD80 and CD86 on BMDCs after 24 h incubation with the CpG ODN. However, the expression of CD80 and CD86 was clearly enhanced in the presence of the CpG-IONP micelles (Figure 6f). In contrast, the levels remained the same as for the unstimulated control when the BMDCs were incubated with the CpG ODN-free IONP micelles.

For effective induction of anti-tumor cytotoxic T lymphocyte (CTL) responses, mature DCs must gain mobility and LN homing ability, which correlates with an increased expression of the chemokine receptor CCR7.[71] Flow cytometry studies showed significantly enhanced expression of CCR7 in BMDCs incubated with CpG-IONP micelles compared to free CpG ODNs.

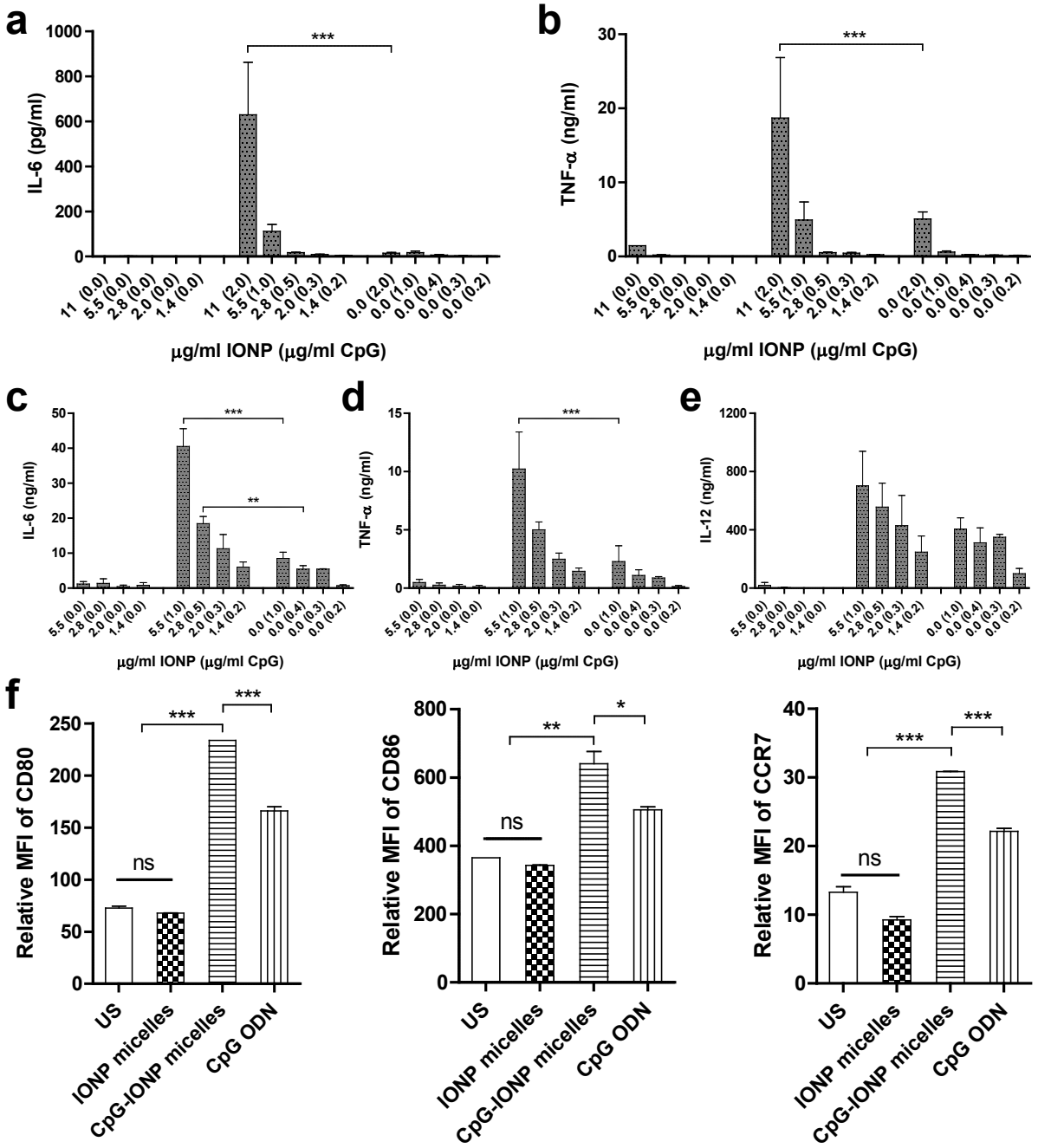


**Figure 6**. Immunostimulatory activity of CpG-IONP micelles *in vitro*. a) IL-6 and b) TNF-α production in J774A.1 macrophages incubated for 24 h with IONP-filled micelles, CpG-IONP micelles or free CpG ODN. c) IL-6, d) TNF-α and e) IL-12 cytokine production in BMDCs incubated for 24 h with IONP-filled micelles, CpG-IONP micelles or free CpG ODN. f) CD80, CD86 and CCR7 mean fluorescence intensity histograms of $CD11c^+$ and MHC $II^+$ double positive unstimulated BMDCs and BMDCs incubated for 24 h with control IONP micelles, CpG-IONP micelles and CpG ODN; 1.4 µg/mL of IONP micelles and 0.2 µg/mL of CpG ODN. Data are presented as mean ± SEM of at least three independent experiments. $^{*}P < 0.05$, $^{**}P < 0.01$,

$^{***}P < 0.001$, ns = non significant by two-way ANOVA followed by Bonferroni's test (a-d) and one-way ANOVA followed by Tukey's test (f).

Systemic application of viral nucleic acids leads to an unspecific, generalized activation of the immune system that may be deleterious. One of the potential advantages of using NPs as delivery vehicle is to abolish systemic release of proinflammatory cytokines whilst providing strong immunostimulatory capacity at target organs such as the spleen and LNs. To examine the unspecific immunostimulatory effect of CpG ODN in the NP vaccine, mice were s.c. injected in the forearm with 3 μg of CpG ODN free and complexed to the IONP-DOTAP micelles (containing 38 μg of magnetite) and with PBS as control. IL-6 levels were measured in the serum of the injected mice at different time intervals. As expected, free CpG strongly increased serum levels of IL-6 already at 4 h post injection. Strikingly, no increase in serum IL-6 levels was observed in mice injected with the CpG-IONP micelles compared to mice treated with PBS (**Figure 7a**). To investigate the targeted effects in the spleen and LNs, the axillary LNs draining the injection site and spleen were harvested and the maturation status of the extracted cells (DCs and Natural Killer cells (NKs)) was analyzed by flow cytometry comparing the expression levels of CD80 and CD86 in DCs and of CD69 in NK cells. The results show that the CpG-IONP micelles are as effective or more than free CpG ODN at promoting maturation of these immune cells in the target secondary lymphoid tissues (Figure 7b-d).

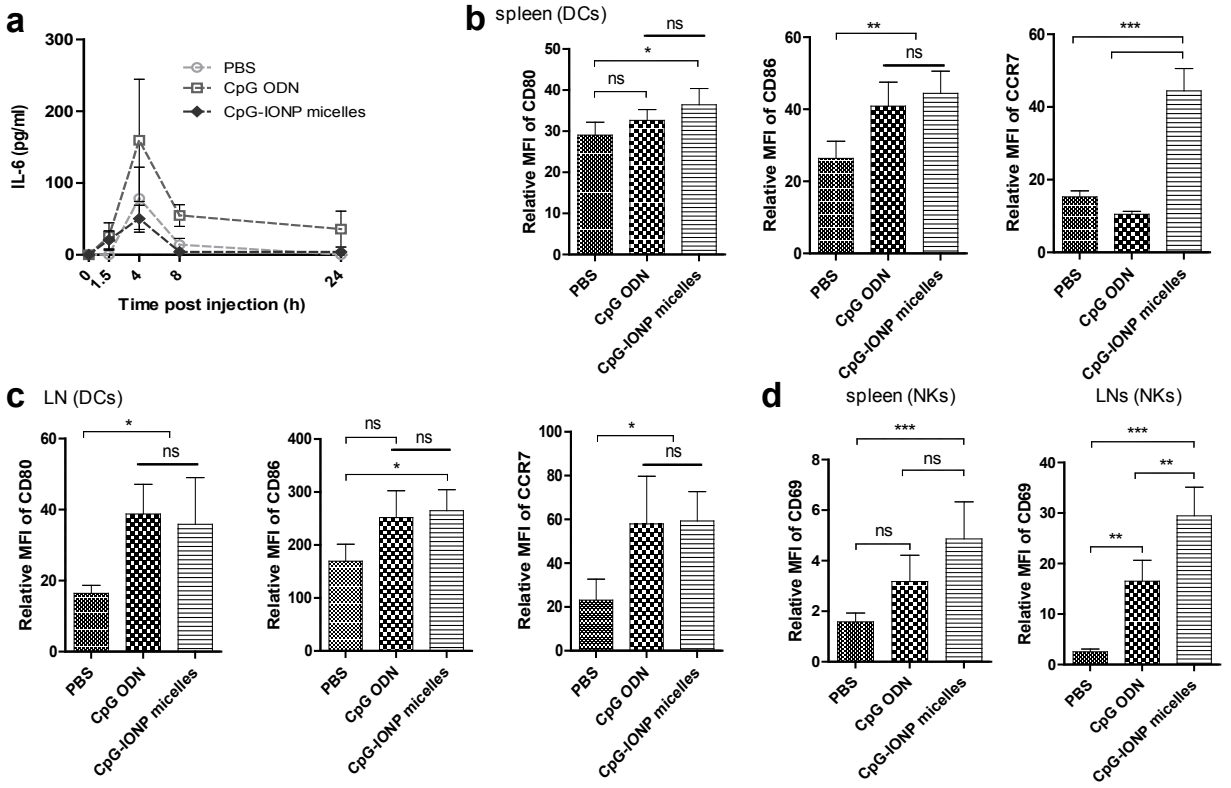


**Figure 7** Comparison of the innate immune responses to CpG ODN and CpG-IONP micelles. C57BL/6 mice were s.c. injected in the forearm with 3 µg of CpG ODNs, free or in conjugation with the IONP-DOTAP micelles (containing 38 µg of magnetite). a) Pro-inflammatory IL-6 cytokine production in blood serum, pre-injection and at several post-injection time points. b-d) Representative CD80, CD86 and CCR7 mean fluorescence intensity histograms of $CD11c^+$ and MHC $II^+$ double positive DCs and of CD69 in NK cells ($CD3^-CD335^+$) extracted from spleen and inguinal LNs of mice 24 h after they were s.c. injected in the forearm with PBS, CpG-IONP micelles and CpG ODN. Data are presented as mean ± SEM of 5 mice per group. $^*P< 0.05$, $^{**}P< 0.01$, $^{***}P< 0.001$, ns = non significant (one-way ANOVA followed by Tukey's test).

Next, we studied the adaptive immune responses that can be achieved *in vivo* using the OVA-IONP micelles compared to free OVA. In response to antigens, naive $CD4^+$ T-cells differentiate into effector T helper (Th) cells, which based on their pattern of cytokine production and their functional responses can be subdivided into those that participate in cell-mediated immune responses (Th1 subset), and those that induce B cells to secrete antibodies (Th2 subset). C57BL/6 and BALB/c mice are the prototypical Th1- and Th2-type mouse strains, respectively. BALB/c mice were immmunized twice (2 weeks between both injections) with 5 µg/mice of

OVA free or as OVA-IONP micelles (containing ca. 53 μg of magnetite) by s.c. injection in the flank or forearm. During 52 days, blood samples were taken every two weeks and analyzed for IgG1 (associated with Th2 responses) and IgG2a (associated with Th1 responses) anti-OVA production (Figure 8). We found that the OVA-specific antibody responses obtained with OVA alone were as expected dominated by IgG1 isotype and very little IgG2a was produced irrespective of the site of injection. IgG2a is considered to be more protective because of its greater capacity to fix complement and to induce antibody-dependent cell-mediated cytotoxicity by macrophages and NKs.[72] Immunization with the OVA-IONP micelles resulted in greatly enhanced IgG1 and IgG2a OVA-specific antibody responses (Figure 8b). This result indicates that the OVA-IONP micelles provide excellent adjuvant effects for cell and humoral immune responses under microdosing conditions. Moreover, even after 52 days when the splenocytes were re-stimulated *ex vivo* in the presence of OVA we found enhanced IFN-γ production in mice previously immunized with the OVA-IONP micelles compared with free OVA (Figure 8c), confirming the good capacity of the IONP micelles for improving adaptive immune responses.

Adjuvants accepted for human use such as alum lack the capacity to generate cell-mediated Th1 immune responses. However, there are a number of diseases, such as cancer and those caused by intracellular pathogens (e.g. HIV and malaria), for which there are no effective prophylactic or therapeutic vaccines and require vaccine formulations that promote a more Th1-like response as opposed to only Th2-like responses. Therefore, these are encouraging *in vivo* results that are in good agreement with earlier reports[19,67] and can be rationalized by the fact that these IONP-based vaccines are delivered directly to the target LNs; that is, they are not taken up by peripheral DCs at the injection site that then migrate to the target LNs, as is the case with the alum-antigen mixtures.

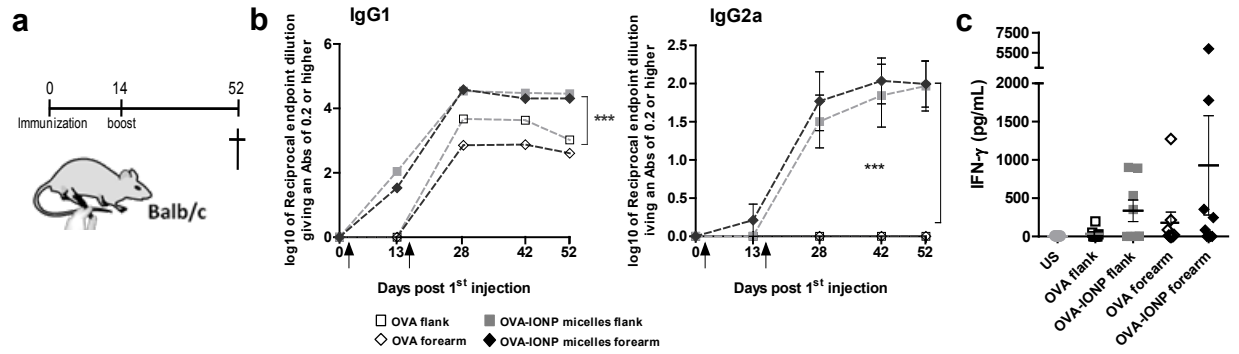


**Figure 8**. Conjugation of OVA to IONP-filled micelles enhances OVA-specific antibody responses. a) Immunization schedule. 5 μg OVA free or in conjugation with the IONP micelles (ca. 53 μg of magnetite) were injected in BALB/c mice on day 0 and 14, subcutaneously in the forearms or in the flanks. Mice were sacrificed on day 52 and splenocytes were harvested for further analysis. b) Anti-OVA IgG1 and IgG2a production in blood serum at different time points after first injection. c) INF-γ production of unstimulated splenoctes (US) or after stimulation in the presence of 10 μg/mL OVA protein. Data are presented as mean ± SEM of 9 mice per group. $^{***}P < 0.001$ by two-way ANOVA followed by Bonferroni's test.

Finally, we evaluated the adaptive immune responses that are achieved *in vivo* administering the OVA-IONP micelles compared to free OVA in conjunction with CpG ODN or CpG-IONP micelles as complementary adjuvant towards providing cellular immunity. A mixture of OVA and alum was injected as comparison with a commercially available adjuvant. $CD8^+$ T cells are considered the subclass of T cells capable of recognising and killing virally infected cells. $CD8^+$ T cells are also emerging to be critical in cancer immunotherapy for their ability to kill autologous cancer cells.[68] The unique ability of $CD8^+$ T cells to kill targets expressing peptide antigens associated with MHC class I underpins their role in providing cellular immunity. In the case of OVA, the peptide SIINFEKL is the MHC-I cytotoxic T cell epitope. High adjuvant doses are generally required to induce strong $CD8^+$ T-cell immunity with subunit vaccines.[16] To investigate the extent to which the TLR 9 ligands at low doses enhances antigen-specific $CD8^+$ T cell responses we used C57BL/6 mice, which were immunized twice (2 weeks between injections) with 5 μg of OVA free or as OVA-IONP micelles alone or combined with only 5 μg of free CpG ODN or delivered by CpG-IONP micelles administered by s.c. injection in the

flanks (with total amount of injected magnetite carrier ca. 7 μg). After 35 days mice were sacrificed and splenocytes were harvested for analyzing the antigen specific $CD8^+$ T cell responses (Figure 9). We could see good potential in co-administering CpG-IONP micelles to induce more robust cellular immunity *in vivo* under microdosing conditions. The proportion of OVA-specific $CD8^+$ T-cells was measured by staining with SIINFEKL-MHC-I dextramer and flow cytometry. We found that only the CpG-IONP micelles were able to provide higher levels of antigen-specific $CD8^+$ T-cells (Figure 9b, c), both in peripheral blood cells and in the spleen. Moreover, when the cell killing potential of the responding $CD8^+$ T-cells was analyzed by flow cytometry by detection of double positive cytotoxic T cells producing both intracellular IFN-γ (an important cytokine required for effective viral clearance) and the degranulation marker CD107a by fluorescence labelling (CD107a-expressing $CD8^+$ T cells have been shown to mediate cytolytic activity in an antigen-specific manner), mice that had been treated with the CpG-IONP micelles gave the best responses (Figure 9d). Further demonstration of the enhanced *in vivo* responses obtained from vaccinated mice that concurrently received CpG-IONP micelles is that spleen cells collected from them produced significantly more IFN-γ following *ex vivo* re-stimulation with SIINFEKL than those vaccinated with OVA alone, OVA + free CpG and OVA-IONP micelles alone (Figure 9f).

Overall, the *in vivo* immunization results demonstrate that developing IONP filled PEG-PL micelles loaded with CpG ODN (as model adjuvant) and OVA (as model antigen) with virtually identical sizes (average diameters of ca. 40 nm) leads to potent and effective cellular and humoral immune responses under micro/nanodosing conditions (3-5 μg of CpG adjuvant, 5 μg of OVA and 7-53 μg of magnetite carrier). The hypothesis/strategy tested was that even if the antigen and adjuvant are on separate NPs (a considerable formulation advantage), the two

payloads are targeted to the same cells because their carriers have the same size (selected to allow efficient delivery to and accumulation within the draining LNs) and therefore delivery behavior. The dose of magnetite carrier required to induce the potent humoral and cellular responses can be considered negligible compared to the normal serum levels of ferritin (12-300 ng/mL), which shows that this is a very effective and safe nano-vaccine. It is expected that microdosing and PET/SPECT imaging, coordinated effectively, will drive and innovate in the new process of DDD allowing safer and fewer animal tests.[75] To the best of our knowledge this is the first vaccine technology integrating these two new DDD methodologies.

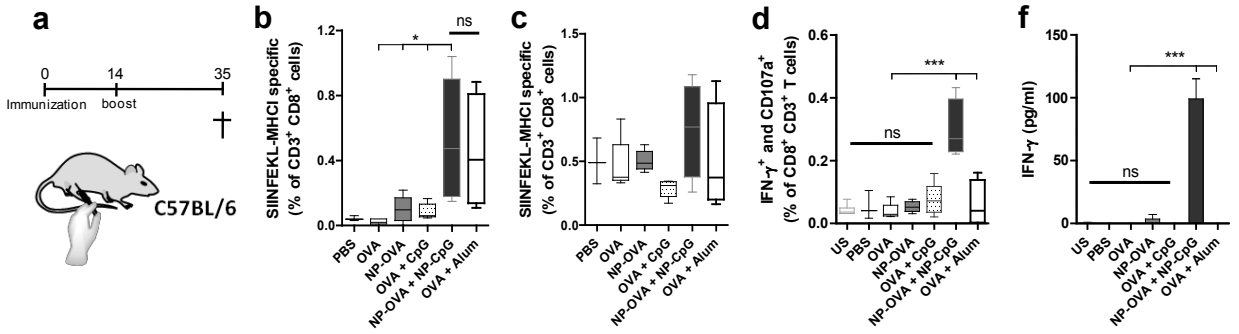


**Figure 9**. Co-administration of OVA-IONP micelles and CpG-IONP micelles enhances cellular immunity *in vivo*. a) Immunization schedule. 5 µg OVA and CpG ODNs free or in conjugation with IONP micelles were injected in C57BL/6 mice subcutaneously in the flank on day 0 and 14; OVA-Alum mixture was included for comparison. Mice were sacrificed on day 35 and primary splenocytes cultures were established for further analysis. Analysis of SIINFEKL pentamer-positive $CD8^+$ T cells in b) peripheral blood cells two weeks after boost (day 28) and c) in spleen after the euthanasia (day 35). d) Intracellular IFN-γ production and degranulation marker CD107a were analyzed by flow cytometry after 5 h *ex vivo* stimulation with SIINFEKL peptide; antigen specific cytotoxic $CD8^+$ T cells were represented as IFN-γ and CD107a double positive cells. f) Extracellular IFN-γ production in spleen after two days stimulation with SIINFEKL peptide. Data are presented as mean ± SEM of 5 mice per group. $^*P < 0.05$, $^{***}P < 0.001$, ns = non significant by one-way ANOVA followed by Tukey's test.

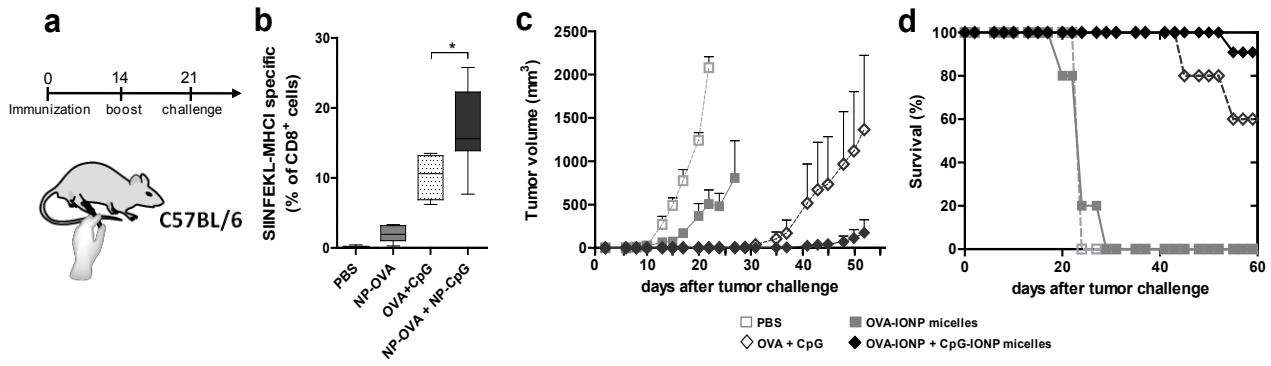


**Figure 10.** Administration of OVA-IONP micelles and CpG-IONP micelles enhances tumor protection in vivo. a) Immunization schedule. 5 µg OVA and CpG ODNs free or in conjugation with IONP micelles were injected in C57BL/6 mice subcutaneously in the right hock on day 0 and 14, as prophylactic agents. On day 21, B16-F10-OVA cells were injected in the right back side and mice were monitored during 60 days. b) Analysis of SIINFEKL pentamer-positive CD8+ T cells in peripheral blood cells one week after boost and just before tumor challenge (day 21). c) Effect of prophylactic immunization on the growth of inoculated tumors and d) survival rate in percentage. Data are presented as mean ± SEM of at least 3 mice per group. *P < 0.05 by one-way ANOVA followed by Tukey's test.

**HAY QUE COMENTAR EL EXPERIMENTO DE TUMORES**

## CONCLUSIONS

Through coordinated and targeted delivery of protein antigen and CpG ODN adjuvant on IONP-filled PEG-PL micelles with an average diameter of ca. 30-45 nm and organic chemistry-free radio-gallium labeling of the magnetite core, we have developed a new class of microdosed nanoparticle-based vaccine which is biocompatible, easy to assemble and combines efficient *in vivo* tracking by $^{67}$Ga SPECT/CT (or PET using $^{68}$Ga) with size-selected properties for accurate delivery to DCs in the LNs.

The present study represents the first example of a radiolabeled antigen and CpG-loaded nanoparticle carrier to monitor *in vivo* delivery and targeting properties by nuclear imaging techniques, which helped to explain and predict its efficacy as synthetic vaccine under microdosing conditions. In terms of radio-gallium labeling, the similarity between $Ga^{3+}$ and $Fe^{3+}$ in charge and size, which results in being readily exchangeable in metallation of biomolecules, could also be conveniently exploited to form stable $^{67}$Ga-magnetite-filled micelles. In this way, high specific activities could be achieved for high sensitivity *in vivo* tracking. Using the lipid-coated IONPs as delivery vehicle of CpG ODNs abolishes systemic release of proinflammatory cytokines. The OVA-IONP micelles enhanced by more than two orders of magnitude IgG1 and IgG2a OVA-specific antibody responses, which demonstrates that the IONP-filled micelle is an effective and versatile antigen vehicle for promoting strong humoral responses. The use of similarly sized IONP also led to better dual-targeting of CpG adjuvant and antigen (co-delivered on separate IONP micelles) in cross-presenting DCs. Coordinating co-delivery of adjuvant and antigen with the lipid-coated IONP vehicles enhanced DC maturation and Th1-cytokine secretion, in turn driving stronger effector cytotoxic antigen-specific $CD8^+$ T lymphocyte (CTL) activation with enhanced cytolytic profiles even with a low dose of adjuvant/antigen. With the

also very low doses (<53 μg/mice) of IONP required for *in vivo* tracking and for eliciting antigen specific immunity this nanoparticle platform seems ideal to develop ultra-high performance non-toxic vaccines.

Although not explored in this study, the use of magnetite NPs offers several further advantages over other NP-based carriers. They are used for hyperthermia therapy,[76] a modality which on its own can be used as an immunotherapy strategy for cancer.[77,78] The use IONP-based vaccines offers the intriguing opportunity of developing novel antitumor therapies which integrate synergistically different antitumor effects and treatment modalities with a simple construct. Additionally, magnetic vaccines could enable drug delivery under a magnetic guidance or actuation mechanism, providing clinicians further spatiotemporal control over the induction of the immune responses. At sufficiently high concentrations the IONPs can also be detected or tracked using high resolution MRI imaging to provide clinicians and drug developers with complementary information (e.g. soft-tissue contrast and high spatial resolution anatomical information) for assessing where or whether the vaccines have been delivered to the target cells/tissue to predict or evaluate therapeutic efficacy. Taken together, these findings and the unique features that set magnetic particles apart from other delivery vehicles suggest that IONP-filled micelles can be expected to be a useful new vaccine technology to tackle infectious diseases and cancer.

## MATERIALS AND METHODS

**Materials**. All experiments were carried out using commercially available reagents, without further purification, unless specified otherwise (Supporting Information).

**Synthesis of CpG-IONP and OVA-IONP micelles.** The synthesis of the oleic acid-coated IONPs (magnetite; $Fe_3O_4$) and water soluble IONP-filled micelles was carried out as described previously.[49] For the synthesis of IONP-filled micelles, different ratios of lipids and IONP-to-lipid ratios were used to optimize the properties (e.g. size and charge) for subsequent attachment of CpG ODNs and OVA. The reported results were obtained with micelles prepared in the following way. Oleic acid-coated magnetite nanoparticle (1 mg) and DPPE-mPEG(2000) (2 mg) and DOTAP (1 mg) or DPPE-mPEG(2000) (1 mg) and DSPE-cPEG(2000) **(**1 mg**)** were dissolved in chloroform (500 µL). After complete evaporation of the chloroform, the dried film was placed 30 s in a water bath at 80 °C and hydrated by adding 500 µL of nanopure water. The solution was transferred to an Eppendorf and centrifuged at 9700 × g for 5 min. The supernatant was passed through a 0.45 µm filter and the resultant solution was centrifuged 3 times at 369,000 × g for 45 min in order to eliminate the empty micelles. Finally, the pellet was dissolved in 400 µL of nanopure water or PBS (10 mM) and stored at RT. For the preparation of fluorescent micelles, DPPE-Rho (at 1-5 % of total moles of lipids) was added to the chloroform solutions containing the PEG PLs and oleic acid-coated $Fe_3O_4$ nanoparticles and the entire synthesis protocol was conducted in the same way but in darkness.

*Attachment of CpG ODNs.* Lyofilized CpG was resuspended in HyClone™ Water, cell culture grade (Thermo Scientific) to a final concentration of 200 µM, aliquoted and stored at -20 °C until use. The IONP-DOTAP micelle stock solution ([IONP] = 2 µM) was mixed with CpG ODNs in

a ratio of 66 moles of CpG ODNs per mole of nanoparticle, in a final volume of 500 μL nanopure water. The mixture was stirred overnight at 700 rpm at RT. The unbound CpG ODNs were eliminated by ultrafiltration through a NanoSep 100k (MWCO 100kDa) centrifugal device (Pall Life Sciences) at 1844 × g for 5 min (3 cycles) and by further ultracentrifugation (369,000 × g, 45 min, 4 cycles). The final pellet was resuspended in the same initial volume of nanopure water or PBS (10 mM) and stored at 4 °C.

*Attachment of ovalbumin.* To the solution of DSPE-cPEG(2000)-containing IONP micelles (stock [IONP] = 3 μM), EDC and NHS in 1:25:15 molar ratio were stirred for 2 h at RT for activation of the carboxylic acid groups. The excess of EDC/NHS was eliminated by ultrafiltration through a NanoSep 100k (MWCO 100kDa) centrifugal device (Pall Life Sciences) (1844 x g for 5 min, 3 cycles). The resulting activated IONP micelles were resuspended in the initial volume and stirred overnight at RT with purified endotoxin-free ovalbumin in a final volume of 300 μL nanopure water. The unbound OVA was eliminated by ultrafiltration at 1844 × g for 5 min (4 cycles). The pellet was resuspended in the initial volume of nanopure water or PBS (10 mM) and stored at 4 °C.

**Characterization of the CpG-IONP and OVA-IONP micelles.** The Fe concentration in the samples was determined by ICP-OES analysis carried out by the SGIker analytical facility of the University of the Basque Country (UPV/EHU; Leioa, Spain). The quantification of bound CpG ODNs was performed by hydrolysis of a known concentration of IONP micelle in the presence of 0.2 M NaOH. The mixture was stirred overnight at RT and ultracentrifudged (369,000 x g, 40 min) to pellet down the disintegrated nanoparticles. The UV-Vis absorbance ($\lambda_{max}$ = 260 nm) of the supernatant was measured using a NanoDrop ND 1000 Spectrophotometer (NanoDrop Technologies) and converted to concentration by comparison to a standard curve. The amount of

OVA bound to IONP-COOH micelles was quantified using a bicinchoninic acid (BCA) protein assay reagent kit (Thermo scientific), after absorbance subtraction of the same concentration of parent IONP-COOH micelles. In this case, the absorbance measurements were performed in a 96-well plate with a TECAN Genios Pro 96/384 multifunction microplate reader. The UV absorption spectra of samples were also measured using NanoDrop ND and a V-630 Bio Spectrophotometer (JASCO Analytical Instruments) and compared against solutions of free OVA/CpG and parent IONP micelles.

Transmission electron microscopy (TEM) studies were conducted on a JEOL JEM-2011 electron microscope operating at 200 kV. The samples were prepared by depositing a drop of a solution of IONPs onto a copper specimen grid coated with a holey carbon film and allowing it to dry. For IONP size determination using TEM, a minimum of 300 particles were measured using the Image J software. Particle size and zeta potential analysis in solution was measured with a NanoSizer (Malvern Nano-Zs, UK). The UV-Vis absorption spectra of the fluorescently labeled IONP micelles were recorded on the V-630 Bio Spectrophotometer and the fluorescence spectra on a NanoDrop ND 3300 Fluorospectrometer (NanoDrop Technologies).

**Labeling of IONP micelles with $^{67}$Gallium.** $^{67}$Ga was purchased as citrate solution from Molypharma (Spain) (specific activity = 1.4 TBq/μmol), and converted into $^{67}GaCl_3$ following a previously reported method.[79] Briefly, the gallium citrate solution was passed through a light silica column cartridge (Sep-Pak®, Waters) to selectively retain the radiometal. The cartridge was washed with ultrapure water (10 mL) and $^{67}$Ga was finally eluted with HCl 0.1 M solution. The eluate was collected in different 100 μL fractions, and only those containing the maximum activity concentration were used in subsequent labeling experiments. The eluted $^{67}$Ga chloride solution (100 μL, c.a. 37 MBq) was then mixed with 50 μL of IONP micelle solution and diluted

up to final volume of 350 μL in acetate buffer (pH = 3.8 ± 0.1). After incubation at 70 °C during 30 min, the reaction crude was cooled down to room temperature and the labeled NPs were separated via centrifugal filtration (6708 × g for 10 min) using AmiconUltracel 100k (MWCO 100kDa) centrifugal devices (Merck), and washed twice with sodium acetate buffered solution. The retentate was recovered from the filter by the addition of nanopure water or 10 mM PBS (100 μL). The total radioactivity in the filtrates and retentates were measured in a CRC-25R dose calibrator (Capintec, USA) in order to determine the incorporation efficiency. For stability studies, one batch of $^{67}$Ga-IONP micelles was fractioned in different aliquots, which were incubated in the presence of DOTA chelating agent ($10^6$ moles of DOTA per mole of nanoparticle) at 37 °C. At different time points, the samples were filtered in order to separate the NPs from the $^{67}$Ga complexed to DOTA, and radioactivity in the retentate and in the filtrate was measured in a 2470 WIZARD2 Automatic Gamma Counter (PerkinElmer). The dissociation of $^{67}$Ga (expressed in percentage) from the radiolabeled micelles at each time point was calculated as the ratio between the amount of radioactivity in the filter and the starting amount of radioactivity.

**Method for bone marrow-derived cells (BMDCs) differentiation.** BALB/c mice (6-12 weeks old) were sacrificed by cervical dislocation and intact femurs and tibiae of hind limbs were removed aseptically. Bones were washed in cold PBS (10mM) and bone marrow was flushed with cold PBS (10 mM) using a syringe as described previously.[69] Clusters within the marrow were disaggregated to get a homogeneous cell suspension and after the erythrocytes were lysed, the cells were washed and resuspended in RPMI-1640 supplemented with penicillin (100 μg/mL), Streptomycin (100 μg/mL), L-glutamine (2 mM) and heat inactivated FBS (10%). On day zero cells were plated at a concentration of $2 \times 10^6$ cells per 100 mm bacteriological petri

dish (Falcon) in 10 mL of media supplemented with 20 ng/mL of murine GM-CSF (Peprotech) and maintained in a humidified incubator with 37°C and 5% $CO_2$. On day 3, 10 mL of complete RPMI media containing GM-CSF (20 ng/mL) was added to each petri dish. On day 6, half of the supernatant was collected, centrifuged and cell pellet resuspended in 10 mL of fresh complete RPMI with GM-CSF (10 ng/mL) and added again to each petri dish. Finally, on day 8-9 cells were harvested and resuspended in complete RPMI at the desired concentration for each experiment. The cells were used to test the uptake, cytotoxicity and the immunostimulatory capacity of different formulations.

**Cellular uptake studies**. *a) Flow cytometry.* J774A.1 cells (ATCC) were plated in 96-well plates ($1 \times 10^5$ cells/well) and allowed to adhere overnight in DMEM supplemented with 5% FBS, 1% PS. Fluorescent formulations containing the DPPE-Rho phospholipid were diluted in media at different concentrations and added to cells, which were maintained at 37 °C, 5 % $CO_2$ during 3 h. BMDC at day 8-9 of the differentiation process were plated in 96-well plates ($2 \times 10^5$cells/well) in the presence of the fluorescent formulations and incubated overnight at 37 °C, 5 % $CO_2$. After the incubation with the formulations, the media was removed and cells were transferred to cytometer tubes in sterile PBS (10 mM) and pellet down by centrifugation (580 x g, 5 min, 4 °C). Cells were resuspended in a final volume of 200 µL of flow cytometry buffer (0.1 % BSA, 0.1% sodium azide in PBS (10 mM)). Rhodamine uptake was measured using a FACS Canto II (BD Biosciences) and the data were analyzed using the FlowJo, LCC software. Both cell types were electronically gated based on the forward and side scatter parameters and the not-single events leaved out based on forward area and height scatter parameters. In the case of the BMDC, cells were gated based on double positive staining for CD11c (APC-labeled anti-CD11c, from BD Bioscience) and MHC class II (PerCP-Cy5.5-labeled anti-IA/IE) population

markers and rhodamine uptake analyzed into this population. *b) Cell imaging.* Cells were plated in an ibidi μ-Slide VI 0.4 ($3 \times 10^4$ J774A.1 cells/channel and $9 \times 10^4$ BMDCs/channel) and allowed to adhere overnight in the presence of complete media (DMEM for J774A.1 and RPMI for BMDC). The media was changed and the cells were incubated with the solution containing CpG- or OVA-IONPs micelles labeled with rhodamine B for up to 3 h. The media was removed and fresh media containing Lysotracker (1 μM) was added. After 45 min, the media was removed, the cells were washed twice with sterile PBS (10 mM) and the complete media was added to preserve the cells. To investigate if the CpG-IONPs micelles target TLR 9, the cells were seeded as above, but after the nanoparticle incubation step, the cells were treated as follows. The media was removed and the adherent cells were fixed and permeabilized for 20 min with BD Cytofix/Cytoperm™ fixation and permeabilization kit at 4 °C. After being washed twice with BD Perm/wash™ buffer, the blocking buffer (10% FBS in 10 mM PBS) was then added for 20 min at room temperature. The cells were incubated overnight at 4 °C with the primary anti-TLR 9 antibody (10 μg/mL) in blocking buffer. Then at room temperature, the cells were washed twice with sterile PBS (10 mM). Alexa488-labeled secondary antibody (1 μg/mL in blocking buffer, 1 h) was used for staining of the primary TLR 9 antibody. Nuclei were stained with DAPI (1 μg/mL in media for J774A.1 cells and 5 μg/mL for BMDC) for 15 min at 37 °C. Cells were visualized using a Zeiss Axio Observer wide field fluorescence microscope (Carl Zeiss, Germany). Brightfield and fluorescence images were collected and processed using AxioVision software.

**Animals**. Animals were cared for and handled in compliance with the Guidelines for Accommodation and Care of Animals (European Convention for the Protection of Vertebrate Animals Used for Experimental and Other Scientific Purposes) and internal guidelines, and all

the experimental procedures were approved by the appropriate local authorities. All animals were housed in ventilated cages and fed on a standard diet *ad libitum.*

**SPECT/CT studies**: BALB/c mice (6-8 weeks old) received injection of $^{67}$Ga-IONP micelles dissolved in PBS (10 mM) via different administration routes: subcutaneous on the inner side of the front forearm (30 µL, 7.7 MBq in the left limb) or into the hock (the lateral tarsal region just above the ankle) (30 µL, 7.3 MBq in the left limb) or in the flank (30 µL, 6.4 MBq in the left side). In each case, with the mouse under isoflurane anaesthesia (1.5-2% in oxygen), whole-body SPECT/CT scans were acquired at 3 h and 24 h post-injection (p.i.). With the full ring detector, 360° of data were acquired by rotating the collimator 45° (45 steps, 1 °/step). Data were collected in an energy window of 125-150 keV and the duration of the scans was 60 min (80 sec/step). During image acquisition, mice were kept normothermic by the use of a heating blanket (Homeothermic Blanket Control Unit; Bruker BioSpin GmbH, Karlsruhe, Germany). After each SPECT scan, CT acquisitions were performed to provide anatomical information of each animal. The CT acquisition consisted of 220 views were acquired in 0.88° increments around the animal with 16 ms exposure per view. The X-ray tube settings were 70 kV and 32 mA. SPECT/CT images were acquired using the eXplore speCZT CT preclinical imaging system (GE Healthcare, USA). The system combines SPECT and CT on one gantry, allowing co-registration of the SPECT and CT datasets without additional post-processing. The SPECT scanner uses a stationary, full ring of CZT detectors and interchangeable rotating cylindrical collimators. An 8-slit collimator was used with a field of view of 32 and 78 mm in the transaxial and axial directions, respectively. The SPECT images were reconstructed using the OSEM iterative algorithm (5 iterations, 15 subsets) into 128 x 128 x 32 array with a voxel size of 0.4 x 0.4 x 2.46 mm, and were not corrected for scatter and attenuation. The CT images were

reconstructed using a cone beam filtered back-projection Feldkamp algorithm into 437 x 437 x 523 array with a voxel size of 0.2 x 0.2 x 0.2 mm. At the end of the scanning procedure, the mice were culled by cervical dislocation and organs of interest removed for further *ex vivo* SPECT/CT imaging under the same conditions of the *in vivo* images. Analysis of the injected dose percentage per organ was performed by measuring their activity with a WIZARD$^2$2470 Automatic Gamma Counter (PerkinElmer).

**Cytotoxicity studies**. Cells were seeded (J774A.1: $3 \times 10^4$ cells/well in phenol red free DMEM media; BMDC: $2 \times 10^5$cells/well in complete RPMI-1640 media containing 20 ng/mL GM-CSF) in 96-well plates (100 μL/well). For the J774A.1 macrophages, cells were allowed to adhere to the plate overnight. Then, media was removed and cells were left untreated or treated with CpG-IONP micelles and the corresponding controls (IONP-DOTAP micelles and free CpG ODNs), diluted accordingly in media, in triplicate. In the case of BMDC, samples to be tested were added directly to the DC containing wells (100 μL/well) diluted accordingly in media, in triplicate. After 24 h incubation at 37 °C cell supernatant was removed and frozen for subsequent cytokine analysis. The cell viability was measured using the MTT assay. Briefly, 100 μL of MTT reagent (0.25 mg/mL in DMEM for J774A.1 or RPMI-1640 in the case of BMDCs) was added per well after the removal of the supernatant. Cells were incubated at 37 °C for 1 h, after which the media was removed and the lysis solution (200 μL of DMSO) was added. The absorbance of samples was measured using a microplate reader at 550 nm and data represented as the cell viability compared to untreated control wells. The experiments were repeated three times.

**Quantification of cytokine and antibody production by ELISA**. Cytokines were measured in cell supernatants or in blood serum using sandwich ELISA. A 4-parameter sigmoidal (logistic) standard curve was used to quantify the cytokine present (GraphPad Prism software). Results are

expressed as mean ± SEM in pg/mL or ng/mL, compared to untreated control wells. Anti-OVA IgG antibodies were measured in blood serum using indirect ELISA. The results were expressed as the $\log_{10}$ value of the reciprocal of the endpoint dilution which gave an optical density (O.D.) higher than the chosen cutoff, after the subtraction of background levels. In both ELISA types, the measurement of each sample was conducted in duplicate.

**BMDC Maturation Assay**. Cells were counted and resuspended in complete RPMI media at a final concentration of $2 \times 10^5$ cells per well (100 µL) in 96-well plates. BMDCs were kept unstimulated or were stimulated with CpG-IONP micelles ([CpG] = 0.2 µg/mL, [IONP] = 1.4 µg/mL), the corresponding amount of parent IONP micelles or free CpG ODNs (added in 100 µL per well) and incubated overnight at 37 °C. BMDCs were stained with APC-labeled anti-CD11c, PerCP-Cy5.5-labeled anti-IA/IE, FITC-labeled anti-CD80, PE-labeled anti-CD86, and Pacific Blue-labeled anti-CCR7 antibodies. The expression of the different molecules was analyzed using the FACS Canto II flow cytometer. The gating strategy was done as previously mentioned and maturation markers expression analyzed in the final gated DC population (double positive for CD11c and IA/IE). Isotype controls were included in each assay and are not included in the figures for clarity purposes.

**Purification of peripheral blood cells.** In order to analyze the circulating SIINFEKL-specific $CD8^+$ T cells, blood was taken (100 µL) via the facial vein and diluted up to 4 mL in cold PBS (10mM). After centrifugation (580 x g, 5 min at 4 °C), the pellet was resuspended in 2 mL of RBC lysis buffer (BD Biosciences) and incubated at room temperature for 15 min. The lysis was quenched by addition of 2 mL of 5% FBS in 10 mM PBS and mixture was washed twice, ready for further analysis.

**Splenocytes and lymphocytes primary culture preparation**. For the analysis of innate and adaptive immune responses induced *in vivo* after immunization, spleens and draining lymph nodes (dLNs) were removed and processed for further analysis *ex vivo*. Briefly, organs were perfused with tissue dissociating mix (3 mL of collagenase/DNase I diluted in RPMI-1640 media), cutted into small pieces (spleen) and incubated for 30 min at room temperature in a sterile Petri dish. The reaction was stopped with 500 mM EDTA and organs were smashed with the plunger of a syringe. Red blood cells lysis was performed in those cell suspensions derived from spleens, by adding 1 mL of RBC lysis buffer (0.15 M of $NH_4Cl$, 10 mM of $KHCO_3$, and 0.1 mM of $Na_2EDTA$ in nanopure water, pH = 7.4, sterile) for 1 min and rapidly quenched with 10 mL of cold PBS (10mM). The resulting cell suspensions were recollected into 15 mL tubes, washed twice with cold PBS and resuspended in complete RPMI-1640, ready for the different studies.

**Assessing innate immune responses *in vivo***. C57BL/6 mice (6–8 weeks old) were injected subcutaneously in both inner sides of the front forearms with the formulations diluted in PBS (10 mM) (20 μL/forearm, 3.2 μg of CpG and 38 μg of IONP per mice). Both pre-injection, and at various time-points thereafter, blood was taken (25 μL) via the facial vein and serum cytokine levels were analyzed by standard sandwich ELISA. After the final blood collection (24 h after injection) mice were sacrificed by cervical dislocation and spleen and axillary LN extracted and processed as described above, for further analysis of the maturation of DC and NK cells. Briefly, $1 \times 10^6$ cells diluted in RPMI-1640 were placed per well in a 96-well plate and divided into two different staining panels. For the DC maturation, cells were stained as described in the *in vitro* assays. In the case of NK panel, cells were stained with Brilliant Violet 421™-labeled anti-CD3, PE-labeled anti-CD335 (NKp46) and APC-labeled anti-CD69 antibodies. NK cells population

was defined as CD3 negative and CD335 positive, and CD69 expression was analyzed into this defined population.

**Assessing adaptive immune responses *in vivo***. Two types of immunization studies were carried out in order to answer different questions. For the OVA-IONP micelles immunization studies, BALB/c mice (6–8 weeks old) were immunized twice with a two weeks interval between both injections. OVA-IONP micelles dissolved in PBS (10 mM) (5 μg of OVA and 53 μg of IONP per mice) were injected via two different routes: s.c. into the inner side of the front forearms (20 μL/forearm) or into the flanks (20 μL/side). Blood was taken (50 μL) via the facial vein at different time-points (pre- and after-injection), and serum was analyzed for the presence of anti-OVA IgG antibodies by standard indirect ELISA. Six weeks after the last immunization, mice were sacrificed by cervical dislocation and splenocytes harvested as described before. In order to analyze the IFN-γ production, $1 \times 10^6$ splenocytes or lymphocytes cells were plated in 96-well plates and incubated for 48 h in the presence of the stimulus (10 μg/mL of OVA) or in combination with IONP micelles). Results are expressed as mean ± SEM of 9 mice per each group of immunization from two independent studies, analyzed individually and compared to unstimulated wells.

In the case of the combination of CpG- and OVA-IONP micelles immunization studies, C57BL/6 mice (6–8 weeks old) were immunized s.c. in the flanks twice with an interval of one week between injections (0.2 mL/mice; 5 μg of CpG; 5 μg of OVA and ca. 6.9 μg of IONP per mice). Blood was taken (100 μL) as previously described; serum was analyzed for the presence of anti-OVA IgG antibodies and peripheral blood cells harvested for further analysis. 35 days after the first injection, mice were sacrificed by cervical dislocation and the splenocytes analyzed for SIINFEKL-specific $CD8^+$ T cells, extracellular and intracellular IFN-γ production and

CD107a degranulation marker expression. The extracellular IFN-γ production was performed as previously described, but placing $8 \times 10^5$ cells/well and incubating the cells for 48 h with 10 μg/mL of SIINFEKL. To study intracellular IFN-γ and the expression of the degranulation marker, $1 \times 10^6$cells/well were placed in a 96-well plate in 100 μl of RPMI media in the presence of BD Golgi Stop™, the PE-labeled anti-CD107a antibody (LAMP-1 protein) and 10 μg/mL SIINFEKL in RPMI-1640 media. After 5 h of incubation at 37 °C, cells were washed twice and stained with the surface marker Brilliant Violet421™-labeled anti-CD3 Brilliant Violet510™-labeled anti-CD4 and PE-Cy7-labeled anti-CD8. Then, cells were fixed and permeabilized as previously described, after which intracellular cytokine staining was performed (APC-labeled anti-INF-γ). T cells were gated based on double positive for CD3 and CD8 markers, excluding $CD4^+$ cells. Results are represented as IFN-γ and CD107a double positive cell percentage of total $CD3^+$ $CD8^+$ T cells. For the analysis of the SIINFEKL-specific T cells, $1 \times 10^6$ splenocytes or peripheral blood cells were stained with Brilliant Violet™421-labeled anti-CD3, PE.Cy7-labeled anti-CD8 and PE-labeled H-$2k^b$-$OVA_{257-264}$ dextramer (Immudex). SIINFEKL-specific cell percentage was analyzed in the $CD3^+$ and $CD8^+$ double positive population. Isotype controls were included in intracellular IFN-γ analysis by flow cytometry assay and are not included in the figures for clarity purposes. Results are expressed as mean ± SEM of 5 mice per group of immunization, analyzed individually and compared to unstimulated wells.

**Prophylactic immunization for tumor challenging *in vivo***. To study the prophylactic effect of the described systems, C57BL/6 mice (6–8 weeks old) were immunized as described in the combination of CpG- and OVA-IONP micelles immunization studies with slight differences (0.04 mL, s.c. in the right hock). One week after the second administration, 380,000 B16-F10-OVA cells were injected in the right back and animals were monitored for tumor growth.

ACKNOWLEDGMENT

This work was financed by Spanish Ministry of Economy and Competitiveness (grants PRI-PIBIN-2011-0812, CTQ2014-54761-R and MAT2013-48169-R), the Department of Industry of the Basque Country (grant ETORTEK). We thank Dr J. Hernandez-Gil for carrying out TEM and DOTA conjugation to QDs, Mikel Gonzalez Esparza for radiolabeling studies and Dr Boguslaw Szczupak and Zuriñe Baz Maldonado for processing and reconstructing the SPECT/CT images. A. R. de A. acknowledges a PhD studentship from the Department of Education, Language Policy and Culture of the Basque Government.

## REFERENCES


(1) Morens, D. M.; Folkers, G. K.; Fauci, A. S. *Nature* **2004**, *430* (6996), 242–249.

(2) Berzofsky, J. a; Ahlers, J. D.; Belyakov, I. M. *Nat. Rev. Immunol.* **2001**, *1* (3), 209–219.

(3) Bonifaz, L. C.; Bonnyay, D. P.; Charalambous, A.; Darguste, D. I.; Fujii, S.-I.; Soares, H.; Brimnes, M. K.; Moltedo, B.; Moran, T. M.; Steinman, R. M. *J. Exp. Med.* **2004**, *199* (6), 815–824.

(4) Dudziak, D.; Kamphorst, A. O.; Heidkamp, G. F.; Buchholz, V. R.; Trumpfheller, C.; Yamazaki, S.; Cheong, C.; Liu, K.; Lee, H.-W.; Park, C. G.; Steinman, R. M.; Nussenzweig, M. C. *Science* **2007**, *315* (5808), 107–111.

(5) Trumpfheller, C.; Finke, J. S.; López, C. B.; Moran, T. M.; Moltedo, B.; Soares, H.; Huang, Y.; Schlesinger, S. J.; Park, C. G.; Nussenzweig, M. C.; Granelli-Piperno, A.; Steinman, R. M. *J. Exp. Med.* **2006**, *203* (3), 607–617.

(6) Kwon, Y. J.; James, E.; Shastri, N.; Fréchet, J. M. J. *Proc. Natl. Acad. Sci. U. S. A.* **2005**, *102* (51), 18264–18268.

(7) Broaders, K. E.; Cohen, J. A.; Beaudette, T. T.; Bachelder, E. M.; Fréchet, J. M. J. *Proc. Natl. Acad. Sci. U. S. A.* **2009**, *106* (14), 5497–5502.

(8) Randolph, G. J.; Angeli, V.; Swartz, M. A. *Nat. Rev. Immunol.* **2005**, *5* (8), 617–628.

(9) Reddy, S. T.; van der Vlies, A. J.; Simeoni, E.; Angeli, V.; Randolph, G. J.; O'Neil, C. P.; Lee, L. K.; Swartz, M. A.; Hubbell, J. A. *Nat. Biotechnol.* **2007**, *25* (10), 1159–1164.

(10) Moon, J. J.; Huang, B.; Irvine, D. J. *Adv. Mater.* **2012**, *24* (28), 3724–3746.

(11) Pashine, A.; Valiante, N. M.; Ulmer, J. B. **2005**.

(12) Krieg, A. M. *Nucleic Acid Ther.* **2012**, *22* (2), 77–89.

(13) Blasius, A. L.; Beutler, B. *Immunity* **2010**, *32* (3), 305–315.

(14) Pohar, J.; Kužnik Krajnik, A.; Jerala, R.; Benčina, M. *J. Immunol.* **2015**, *194* (8), 3901–3908.

(15) Tao, Y.; Ju, E.; Li, Z.; Ren, J.; Qu, X. *Adv. Funct. Mater.* **2014**, *24* (7), 1004–1010.

(16) De Titta, A.; Ballester, M.; Julier, Z.; Nembrini, C.; Jeanbart, L.; van der Vlies, A. J.; Swartz, M. a; Hubbell, J. a. *Proc. Natl. Acad. Sci. U. S. A.* **2013**, *110*, 19902–19907.

(17) Lin, A. Y.; Mattos Almeida, J. P.; Bear, A.; Liu, N.; Luo, L.; Foster, A. E.; Drezek, R. A. *PLoS One* **2013**, *8* (5).

(18) Bourquin, C.; Anz, D.; Zwiorek, K.; Lanz, A.-L.; Fuchs, S.; Weigel, S.; Wurzenberger, C.; von der Borch, P.; Golic, M.; Moder, S.; Winter, G.; Coester, C.; Endres, S. *J. Immunol.* **2008**, *181*, 2990–2998.

(19) Lee, I.-H.; Kwon, H.-K.; An, S.; Kim, D.; Kim, S.; Yu, M. K.; Lee, J.-H.; Lee, T.-S.; Im, S.-H.; Jon, S. *Angew. Chem. Int. Ed. Engl.* **2012**, *51* (35), 8800–8805.

(20) Moon, J. J.; Suh, H.; Bershteyn, A.; Stephan, M. T.; Liu, H.; Huang, B.; Sohail, M.; Luo, S.; Um, S. H.; Khant, H.; Goodwin, J. T.; Ramos, J.; Chiu, W.; Irvine, D. J. *Nat. Mater.* **2011**, *10* (3), 243–251.

(21) Hubbell, J. a; Thomas, S. N.; Swartz, M. a. *Nature* **2009**, *462* (7272), 449–460.

(22) Kasturi, S. P.; Skountzou, I.; Albrecht, R. A.; Koutsonanos, D.; Hua, T.; Nakaya, H. I.; Ravindran, R.; Stewart, S.; Alam, M.; Kwissa, M.; Villinger, F.; Murthy, N.; Steel, J.; Jacob, J.; Hogan, R. J.; García-Sastre, A.; Compans, R.; Pulendran, B. *Nature* **2011**, *470* (7335), 543–547.

(23) Wilson, J. T.; Keller, S.; Manganiello, M. J.; Cheng, C.; Lee, C.-C.; Opara, C.; Convertine, A.; Stayton, P. S. *ACS Nano* **2013**, *7* (5), 3912–3925.

(24) Willmann, J. K.; van Bruggen, N.; Dinkelborg, L. M.; Gambhir, S. S. *Nat. Rev. Drug Discov.* **2008**, *7* (7), 591–607.

(25) Rudin, M.; Weissleder, R. *Nat. Rev. Drug Discov.* **2003**, *2* (2), 123–131.

(26) Cunha, L.; Szigeti, K.; Mathé, D.; Metello, L. F. *Drug Discov. Today* **2014**.

(27) Chen, N.; Wei, M.; Sun, Y.; Li, F.; Pei, H.; Li, X.; Su, S.; He, Y.; Wang, L.; Shi, J.; Fan, C.; Huang, Q. *Small* **2014**, *10* (2), 368–375.

(28) Hainfeld, J. F.; O'Connor, M. J.; Dilmanian, F. A.; Slatkin, D. N.; Adams, D. J.; Smilowitz, H. M. *Br. J. Radiol.* **2011**, *84* (1002), 526–533.

(29) Colombo, M.; Carregal-Romero, S.; Casula, M. F.; Gutiérrez, L.; Morales, M. P.; Böhm, I. B.; Heverhagen, J. T.; Prosperi, D.; Parak, W. J. *Chem. Soc. Rev.* **2012**, *41* (11), 4306–4334.

(30) Gao, J.; Gu, H.; Xu, B. *Acc. Chem. Res.* **2009**, *42* (8), 1097–1107.

(31) Na, H. Bin; Song, I. C.; Hyeon, T. *Adv. Mater.* **2009**, *21* (21), 2133–2148.

(32) Weissleder, R.; Moore, A.; Mahmood, U.; Bhorade, R.; Benveniste, H.; Chiocca, E. A.; Basilion, J. P. *Nat. Med.* **2000**, *6* (3), 351–355.

(33) Lee, J.-H.; Huh, Y.-M.; Jun, Y.; Seo, J.; Jang, J.; Song, H.-T.; Kim, S.; Cho, E.-J.; Yoon, H.-G.; Suh, J.-S.; Cheon, J. *Nat. Med.* **2007**, *13* (1), 95–99.

(34) Kim, T.; Momin, E.; Choi, J.; Yuan, K.; Zaidi, H.; Kim, J.; Park, M.; Lee, N.; McMahon, M. T.; Quinones-Hinojosa, A.; Bulte, J. W. M.; Hyeon, T.; Gilad, A. A. *J. Am. Chem. Soc.* **2011**, *133* (9), 2955–2961.

(35) Torres Martin de Rosales, R.; Tavaré, R.; Paul, R. L.; Jauregui-Osoro, M.; Protti, A.; Glaria, A.; Varma, G.; Szanda, I.; Blower, P. J. *Angew. Chem. Int. Ed. Engl.* **2011**, *50* (24), 5509–5513.

(36) Ogawa, K.; Mukai, T.; Inoue, Y.; Ono, M.; Saji, H. *J. Nucl. Med.* **2006**, *47* (12), 2042–2047.

(37) Torres Martin de Rosales, R.; Tavaré, R.; Glaria, A.; Varma, G.; Protti, A.; Blower, P. J. *Bioconjug. Chem.* **2011**, *22* (3), 455–465.

(38) Lewin, M.; Carlesso, N.; Tung, C. H.; Tang, X. W.; Cory, D.; Scadden, D. T.; Weissleder, R. *Nat. Biotechnol.* **2000**, *18* (4), 410–414.

(39) Jarrett, B. R.; Gustafsson, B.; Kukis, D. L.; Louie, A. Y. *Bioconjug. Chem.* **2008**, *19* (7), 1496–1504.

(40) Lee, H.-Y.; Li, Z.; Chen, K.; Hsu, A. R.; Xu, C.; Xie, J.; Sun, S.; Chen, X. *J. Nucl. Med.* **2008**, *49* (8), 1371–1379.

(41) Glaus, C.; Rossin, R.; Welch, M. J.; Bao, G. *Bioconjug. Chem.* **2010**, *21* (4), 715–722.

(42) Patel, D.; Kell, A.; Simard, B.; Xiang, B.; Lin, H. Y.; Tian, G. *Biomaterials* **2011**, *32* (4), 1167–1176.

(43) Boros, E.; Bowen, A. M.; Josephson, L.; Vasdev, N.; Holland, J. P. *Chem. Sci.* **2014**, *6* (1), 225–236.

(44) Chen, F.; Ellison, P. A.; Lewis, C. M.; Hong, H.; Zhang, Y.; Shi, S.; Hernandez, R.; Meyerand, M. E.; Barnhart, T. E.; Cai, W. *Angew. Chem. Int. Ed. Engl.* **2013**, *52* (50), 13319–13323.

(45) Goel, S.; Chen, F.; Ehlerding, E. B.; Cai, W. *Small* **2014**, *10* (19), 3825–3830.

(46) Chakravarty, R.; Valdovinos, H. F.; Chen, F.; Lewis, C. M.; Ellison, P. A.; Luo, H.; Meyerand, M. E.; Nickles, R. J.; Cai, W. *Adv. Mater.* **2014**, *26* (30), 5119–5123.

(47) Sun, S.; Zeng, H.; Robinson, D. B.; Raoux, S.; Rice, P. M.; Wang, S. X.; Li, G. *J. Am. Chem. Soc.* **2004**, *126* (1), 273–279.

(48) Gomez Blanco, N.; Jauregui-Osoro, M.; Cobaleda-Siles, M.; Maldonado, C. R.; Henriksen-Lacey, M.; Padro, D.; Clark, S.; Mareque-Rivas, J. C. *Chem. Commun. (Camb).* **2012**, *48* (35), 4211–4213.

(49) Cobaleda-siles, M.; Henriksen-lacey, M.; Ruiz De Angulo, A.; Bernecker, A.; Vallejo, V. G.; Szczupak, B.; Llop, J.; Pastor, G.; Plaza-garcia, S.; Jauregui-osoro, M.; Meszaros, L. K.; Mareque-rivas, J. C. *Small* **2014**, *10* (24), 5054–5067.

(50) Smith, D. M.; Simon, J. K.; Baker, J. R. *Nat. Rev. Immunol.* **2013**, *13* (August), 592–605.

(51) Manolova, V.; Flace, A.; Bauer, M.; Schwarz, K.; Saudan, P.; Bachmann, M. F. *Eur. J. Immunol.* **2008**, *38* (Lcmv), 1404–1413.

(52) Kamaly, N.; Xiao, Z.; Valencia, P. M.; Radovic-Moreno, A. F.; Farokhzad, O. C. *Chem. Soc. Rev.* **2012**, *41* (7), 2971–3010.

(53) Velikyan, I. *Theranostics* **2013**, *4* (1), 47–80.

(54) Hwang, D. W.; Ko, H. Y.; Lee, J. H.; Kang, H.; Ryu, S. H.; Song, I. C.; Lee, D. S.; Kim, S. *J. Nucl. Med.* **2010**, *51* (1), 98–105.

(55) Zambre, A.; Silva, F.; Upendran, A.; Gano, L.; Paulo, A.; Kannan, R. *J. Nucl. Med.* **2014**, *55* (supplement_1), 1386 – .

(56) Xing, Y.; Zhao, J.; Conti, P. S.; Chen, K. *Theranostics* **2014**, *4* (3), 290–306.

(57) Maldonado, C. R.; Gómez-Blanco, N.; Jauregui-Osoro, M.; Brunton, V. G.; Yate, L.; Mareque-Rivas, J. C. *Chem. Commun. (Camb).* **2013**, *49*, 3985–3987.

(58) Hu, H.; Huang, P.; Weiss, O. J.; Yan, X.; Yue, X.; Zhang, M. G.; Tang, Y.; Nie, L.; Ma, Y.; Niu, G.; Wu, K.; Chen, X. *Biomaterials* **2014**, *35* (37), 9868–9876.

(59) Berry, D. J.; Ma, Y.; Ballinger, J. R.; Tavaré, R.; Koers, A.; Sunassee, K.; Zhou, T.; Nawaz, S.; Mullen, G. E. D.; Hider, R. C.; Blower, P. J. *Chem. Commun. (Camb).* **2011**, *47* (25), 7068–7070.

(60) Carion, O.; Mahler, B.; Pons, T.; Dubertret, B. *Nat. Protoc.* **2007**, *2* (10), 2383–2390.

(61) Shannon, R. D. *Acta Crystallogr. Sect. A* **1976**, *32* (5), 751–767.

(62) Bernstein, L. R. *Pharmacol. Rev.* **1998**, *50* (4), 665–682.

(63) Sun, H.; Li, H.; Sadler, P. J. *Chem. Rev.* **1999**, *99* (9), 2817–2842.

(64) Kaneko, Y.; Thoendel, M.; Olakanmi, O.; Britigan, B. E.; Singh, P. K. *J. Clin. Invest.* **2007**, *117* (4), 877–888.

(65) Jewell, C. M.; López, S. C. B.; Irvine, D. J. *Proc. Natl. Acad. Sci. U. S. A.* **2011**, *108* (38), 15745–15750.

(66) Xie, Y.; Bagby, T. R.; Cohen, M. S.; Forrest, M. L. *Expert Opin. Drug Deliv.* **2009**, *6* (8), 785–792.

(67) Harrell, M. I.; Iritani, B. M.; Ruddell, A. **2008**, *332* (Swartz 2001), 170–174.

(68) Harrell, M. I.; Iritani, B. M.; Ruddell, A. *Am. J. Pathol.* **2007**, *170* (2), 774–786.

(69) Mellman, I.; Steinman, R. M. *Cell* **2001**, *106* (3), 255–258.

(70) Cavanagh, L. L.; Von Andrian, U. H. *Immunol. Cell Biol.* **2002**, *80* (5), 448–462.

(71) Adema, G. J.; de Vries, I. J. M.; Punt, C. J. A.; Figdor, C. G. *Curr. Opin. Immunol.* **2005**, *17* (2), 170–174.

(72) Nimmerjahn, F. *Science (80-. ).* **2005**, *310* (5753), 1510–1512.

(73) Li, H.; Li, Y.; Jiao, J.; Hu, H.-M. *Nat. Nanotechnol.* **2011**, *6* (10), 645–650.

(74) Yee, C.; Thompson, J. A.; Byrd, D.; Riddell, S. R.; Roche, P.; Celis, E.; Greenberg, P. D. *Proc. Natl. Acad. Sci. U. S. A.* **2002**, *99* (25), 16168–16173.

(75) Sugiyama, Y.; Yamashita, S. *Adv. Drug Deliv. Rev.* **2011**, *63* (7), 494–502.

(76) Lee, J.-H.; Jang, J.-T.; Choi, J.-S.; Moon, S. H.; Noh, S.-H.; Kim, J.-W.; Kim, J.-G.; Kim, I.-S.; Park, K. I.; Cheon, J. *Nat. Nanotechnol.* **2011**, *6* (7), 418–422.

(77) Skitzki, J. J.; Repasky, E. A.; Evans, S. S. *Curr. Opin. Investig. Drugs* **2009**, *10* (6), 550–558.

(78) Toraya-Brown, S.; Fiering, S. *Int. J. Hyperthermia* **2014**, *30* (8), 531–539.

(79) Ščasnár, V.; van Lier, J. E. *Eur. J. Nucl. Med.* **1993**, *20* (3), 273–273.

(80) Lutz, M. B.; Kukutsch, N.; Ogilvie, a L.; Rössner, S.; Koch, F.; Romani, N.; Schuler, G. *J. Immunol. Methods* **1999**, *223*, 77–92.

**Supporting Information**: Supporting experimental results, Figures S1-S10. This material is available free of charge via the Internet at http://pubs.acs.org.

**Materials**. Hexane (99%; LABSCAN), chloroform (water 0.005%; LABSCAN), diphenyl ether (99%; Sigma Aldrich), dibenzyl ether (>98%; Alfa Aesar) were purchased from Sigma Aldrich, 1,2-hexadecanediol (>98%; Tokyo Chemical Industry Co. Ltd), oleic acid (90%; Alfa Aesar), oleylamine (70%; Sigma Aldrich), iron(III) acetylacetonate (99%; Strem Chemicals).1,2-Dipalmitoyl-sn-glycero-3-phosphoethanolamine-N-[methoxy(polyethylene glycol)-2000] (ammonium salt) (PEG-OMe), 1,2-distearoyl-sn-glycero-3-phosphoethanolamine-N-[carboxy(polyethylene glycol)-2000] (ammonium salt) (PEG-COOH), 1,2-dipalmitoyl-3-trimethylammonium-propane (chloride salt) (DOTAP), and 1,2-dipalmitoyl-sn-glycero-3-phosphoethanolamine-N-(lissaminerhodamine B sulfonyl) (DPPE-Rho) were purchased from Avanti Polar Lipids. CpG ODNs with the sequence (5'-TCCATGACGTTCCTGATGC-3') was manufactured in the laboratories of The Midland Certified Reagent Company Inc. Albumin from chicken egg white was purchased from Sigma Aldrich and further purified to eliminate endotoxins using an ÄKTA purifier chromatography system, using a Superdex200, 10/300 GL column (GE Healthcare) and UNICORN 5.11 software. 1-Ethyl-3-[-3-dimethylaminopropyl]carbodiimide hydrochloride (EDC) and N-hydroxysulfosuccinimide (sodium salt) (NHSS) were purchased fromThermoscientific. $^{67}$Ga citrate solution was purchased from MOlypharma (Spain) and 1,4,7,10-tetraazacyclododecane-1,4,7,10-tetraacetic acid (DOTA) from Macrocyclics (Inc. Dallas, USA). Dulbecco's Modified Eagle's Medium (DMEM) supplemented with L-glutamine both with and without phenol red, fetal bovine serum (FBS), Penicillin-Streptomycin and L-Glutamine (all of them from Gibco®) were purchased from Life technologies (Thermo Fisher Scientific). RPMI-1640 without L-Glutamine from Lonza. 4',6-

Diamidino-2-phenylindole dihydrochloride (Invitrogen), Lysotracker Green (Molecular Probes), BD Cytofix/CytopermTM Plus Fixation/Permeabilization Kit (BD Biosciences). Anti-TLR 9 and Alexa488 secondary antibody from Abcam. All fluorescently labeled monoclonal antibodies and their respective isotype controls were purchased from BioLegend unless specified otherwise. The Fc blocking antibody was purchased from BD Biosciences and bovine serum albumin (≥ 98%, BSA) from Sigma Aldrich. Neutral Red assay reagent (NR, Sigma Aldrich) and Cell proliferation kit I (MTT, Roche). The ELISA kits for cytokines production analysis were purchased from: R&D Systems (IL-6 kit); PeproTech (IL-12 and TNF-α kit) and BioLegend (INF-γ kit). Goat anti-mouse IgG1- and IgG2a-HRP conjugated antibodies were purchased from AbDSerotec (Bio-Rad). Collagenase D and DNase were purchased from Roche and RBC lysis buffer from BD Bioscience. SIINFEKL OVA peptide (257-264) was purchased from Peptides International and Imject® Alum (Thermo Scientific) was prepared and used as described in the data sheet.

**Nanoparticle Calculations**

In this study we used spherical IONPs (magnetite; $Fe_3O_4$) with an average diameter of 6.767 ± 1.170 nm (Figure S1):

V (IONP) = $4/3 \cdot \pi \cdot r^3 = 4/3 \cdot \pi \cdot (3.3835 \times 10^{-7})^3 = 1.6225 \times 10^{-19}$ $cm^3$; ρ (magnetite) = 5.17 $g \cdot cm^{-3}$; m = ρ (magnetite) · V (IONP) = $8.3884 \times 10^{-19}$ g

moles of $Fe_3O_4$= m / MW ($Fe_3O_4$) = $8.39 \times 10^{-19} / 231.533 = 3.6230 \times 10^{-21}$

moles of Fe = 3 · moles of $Fe_3O_4 = 3 \cdot 3.6230 \times 10^{-21} = 1.0869 \times 10^{-20}$

atoms of Fe per IONP = mole Fe in IONP · $N_A = 1.0869 \times 10^{-20} \cdot 6.022 \times 10^{23} = 6545$

The number of molecules ofligandper IONP was calculated by determining the concentration of Fe of the IONP micelles and ligand-IONP micelles by ICP and assuming that each IONP contains 6545 atoms of Fe**.**

TEM characterization and DLS studies confirmed the size of the different IONP micelles can be controlled and is very similar, which is a key determinant of nanoparticle *in vitro* and *in vivo* drug payload delivery features.

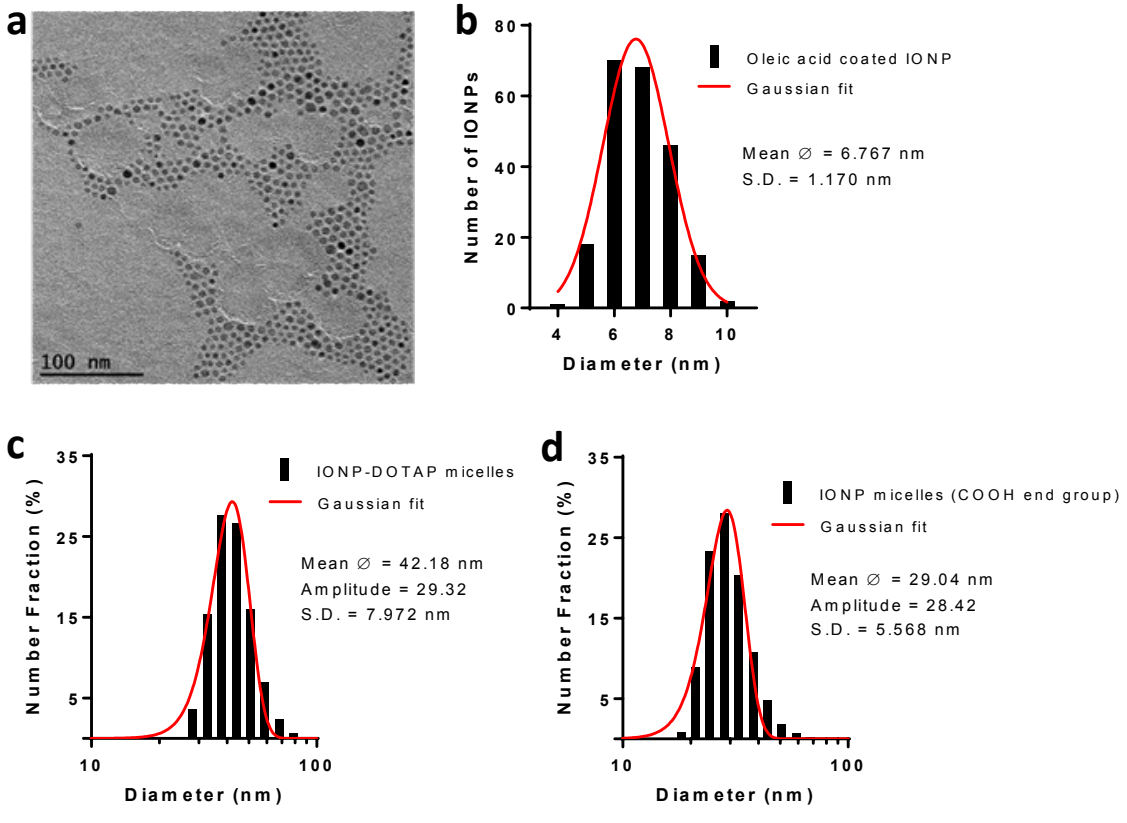


**e**

| | Oleic acid coated IONP | IONP-DOTAP micelles | CpG-IONP micelles (DOTAP) | IONP micelles (COOH) | OVA-IONP micelles (COOH) |
|---|---|---|---|---|---|
| Mean Ø | 6.767 | 42.18 | 43.25 | 29.04 | 32.84 |
| S:D: | 1.170 | 7.972 | 8.970 | 5.568 | 6.905 |

**Figure S1**. Size characterization of the magnetite nanoparticles/micelles. a) Representative TEM image of the hydrophobic IONPs and b) the size distribution of more than 200 NPs. DLS size measurements of c) IONP-DOTAP micelles used to prepared CpG-IONP micelles and d) IONP micelles (with COOH end groups) used to prepare OVA-IONP micelles. e) Comparison of sizes of oleic acid-coated magnetite NPs and corresponding IONP-filled PEG PL micelles before and after biofunctionalization with adjuvant and antigen.

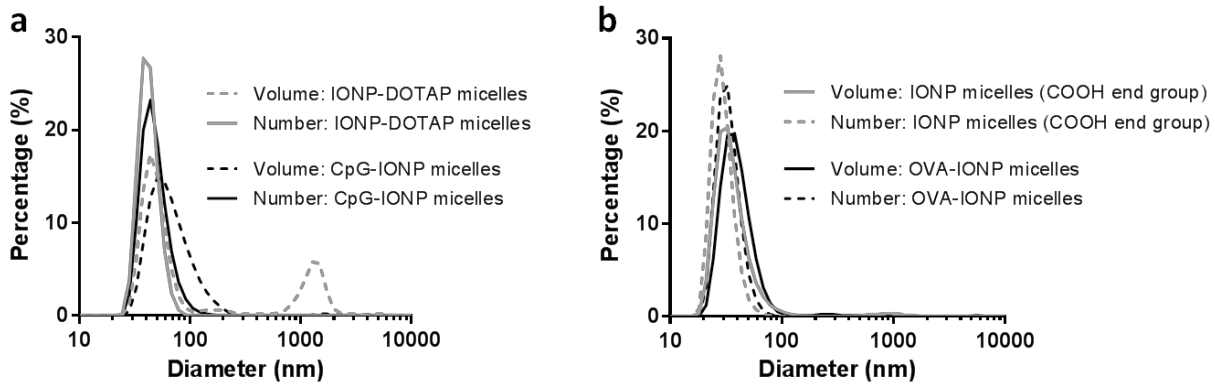


c

| | IONP-DOTAP micelles | CpG-IONP micelles (DOTAP) | IONP micelles (COOH) | OVA-IONP micelles (COOH) |
|---|---|---|---|---|
| Mean Ø | +15.27 | -16.84 | -15.88 | -17.0 |
| S:D: | 0.493 | 1.384 | 1.953 | 2.046 |

**Figure S2.** DLS size and zeta potential comparison of a) IONP-DOTAP micelles before and after biofunctionalization with CpG ODNs and b) IONP micelles containing COOH end group with and without OVA antigen.

Both J774A.1 macrophages cell line and bone marrow derived DCs expressed the toll like receptor 9 (TLR 9).

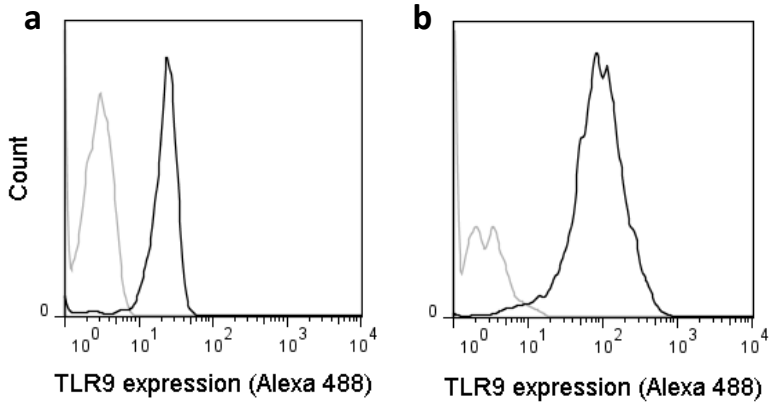


**Figure S3.** Toll like receptor 9 (TLR 9) expression analyzed by flow cytometry in a) J774A.1 macrophages cell line and b) mouse bone marrow derived cells (BMDCs). Non stained control cells (light line) and the cells stained with Alexa Fluor 488-labeled secondary antibody used to visualized TLR 9 (dark line) are shown.

The incorporation of 5% DPPE-Rho does not affect the size of the IONP micelles.

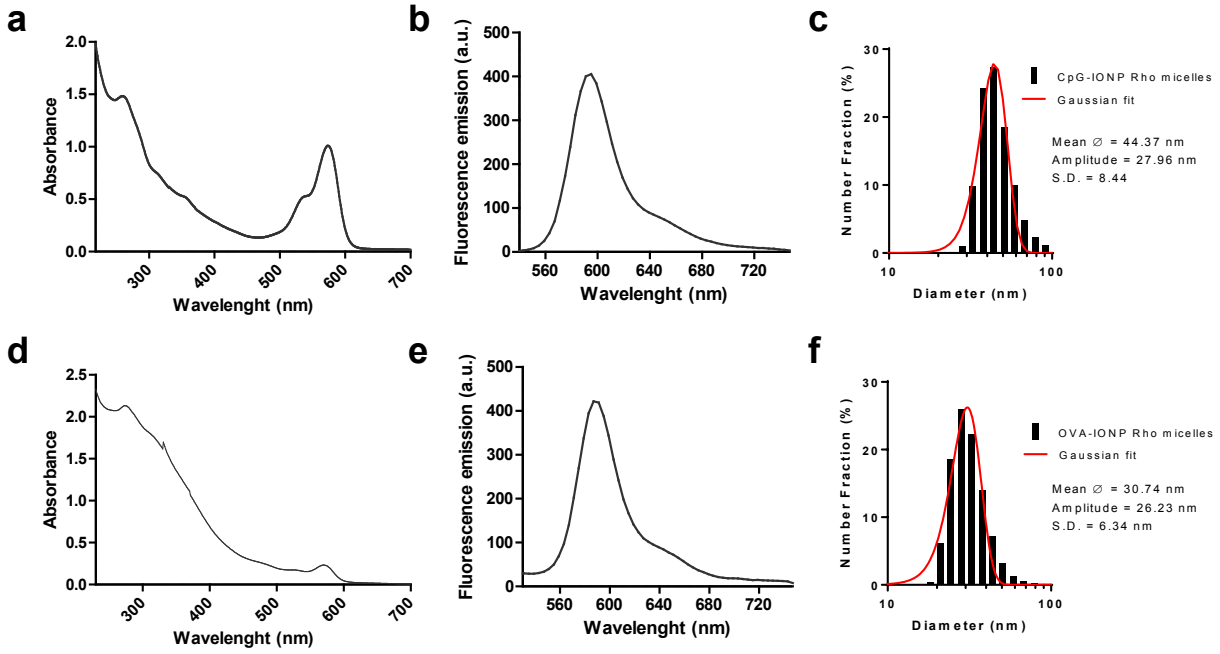


**Figure S4.** Characterization of the OVA-IONP and CpG IONP micelles fluorescently labeled with 5% N-lissamine rhodamine dipalmitoylphosphatidylethanolamine (DPPE-Rho). UV-Vis spectra of a) CpG- and d) OVA-IONP micelles with DPPE-Rho. Fluorescence spectrum of b) CpG- and e) OVA-IONP micelles with DPPE-Rho. Size distribution obtained by DLS of fluorescently-labeled c) CpG-IONP and f) OVA-IONP micelles.

Confirmation by *ex vivo* analysis of the biodistribution of the IONP micelles 24 h after injection in the forearm or in the hock.

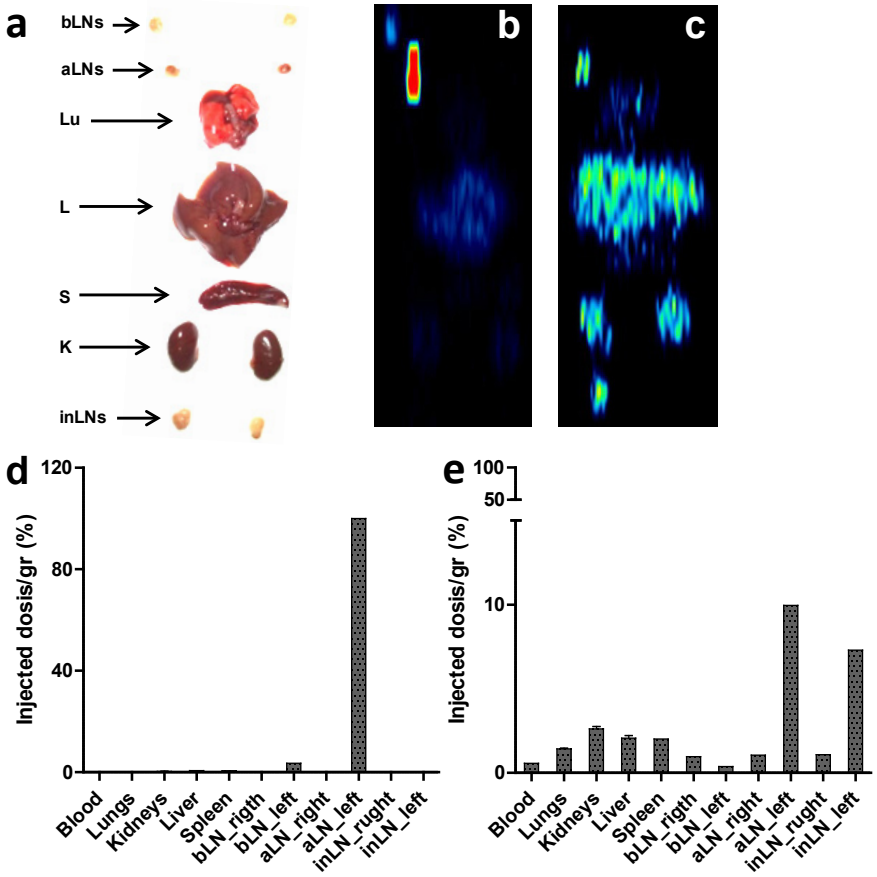


**Figure S5.** *Ex vivo* analysis of the biodistribution after 24 h. a) Photograph of selected harvested organs, SPECT/CT image of the harvested organs when injected in the b) forearm or in the c) hock. Biodistribution expressed as percent injected dose per gram of tissue in the d) forearm or e) hock injection route. bLN, braquial LN; aLN, axillary LN; Lu, lungs; L, liver; S, spleen; K, kidneys; inLN, inguinal LN.

IONP-DOTAP micelles both free and biofuctionalized with CpG ODNs were not toxic at any of the explored IONP concentrations.

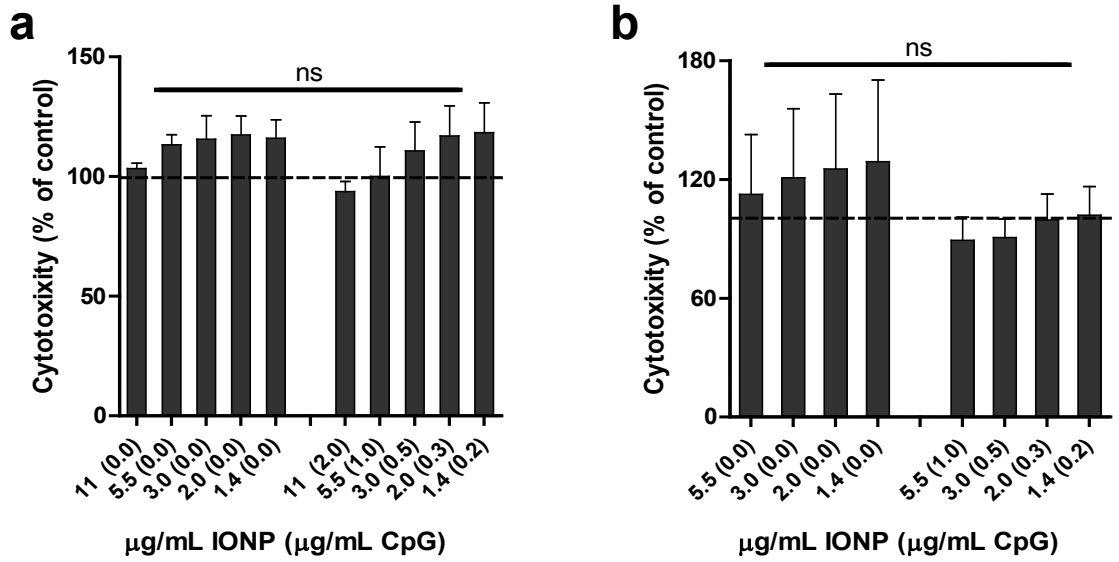


**Figure S6**. Cytotoxicity analysis of CpG-IONP micelles and parent IONP-DOTAP micelles in a) J774A.1 macrophages and b) BMDCs, after 24 h incubation at 37°C. Data are presented as mean ± SEM of three replicates and representative of three separate experiments. ns = non significant by two-way ANOVA followed by Bonferroni's test.

Free CpG ODNs are considerably less inmunostimulatory in J774A.1 macrophages and BMDCs than CpG-IONP micelles (see Figure 6)

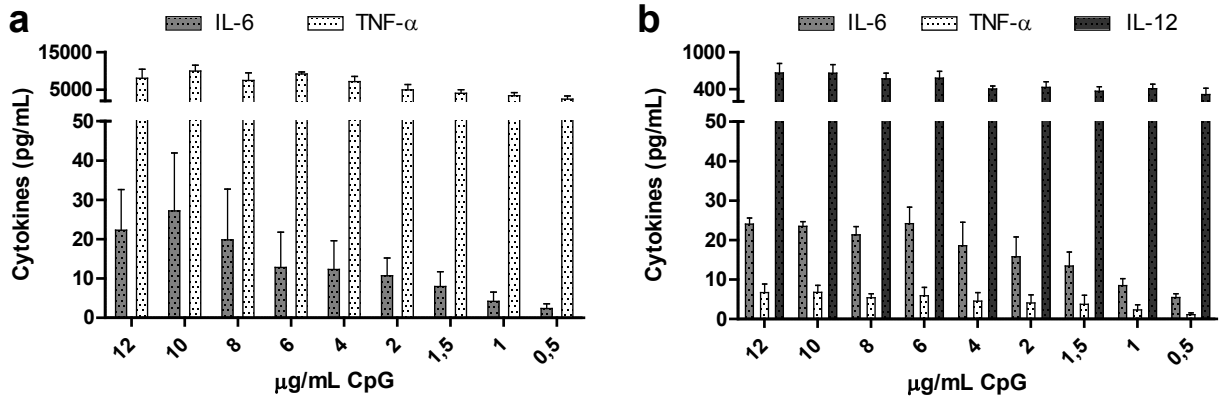


**Figure S7**. Cytokine production in a) J774A.1 macrophages and b) BMDCs after 24 h incubation at 37°C with free CpG ODNs. Data are presented as mean ± SEM of three replicates and representative of three separate experiments.

The stimulation of BMDC with CpG-IONP micelles did not cange the percentage of DCs expressing high levels of MHC class II. When injecting the CpG-IONP micelles in C57bl/6 (3 µg CpG and 20 ng IONP per mice) there was no change in the percentages of mature DCs between groups.

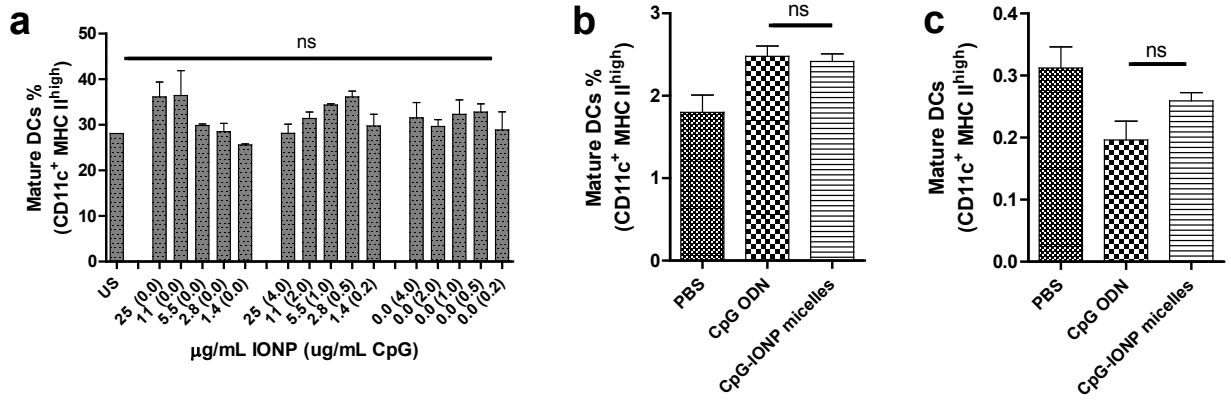


**Figure S8**. a) *In vitro* study of mature DCs after the stimulation of BMDCs over 24 h with IONP micelles, CpG-IONP micelles, CpG free or unstimulated (US). *In vivo* stimulation of innate system by injection of PBS as control, CpG ODNs or CpG-IONP micelles. 24 h after injection, mature DCs percentages were analyzed in b) spleen and c) draining lymph nodes. Data are presented as mean ± SEM of a) 3 independent experiments and b, c) 5 mice per group. ns = non significant by a) two-way ANOVA followed by Bonferroni's test and b, c) one-way ANOVA followed by Tukey's test.

To gain further information about antigen specific antibody production, we analyzed the antibodies in blood serum after the immunization studies combining of CpG- and OVA-IONP micelles. Alum adjuvant totally failed in inducing IgG2c isotype and did not showed significant differences with CpG-IONP micelles in total IgG or IgG1 productions. Overall, when comparing the different adjuvant types (CpG free, CG-IONP micelles and commercially available alum), it was clear that the CpG based systems were the only ones that could trigger a more balanced Th1 response.

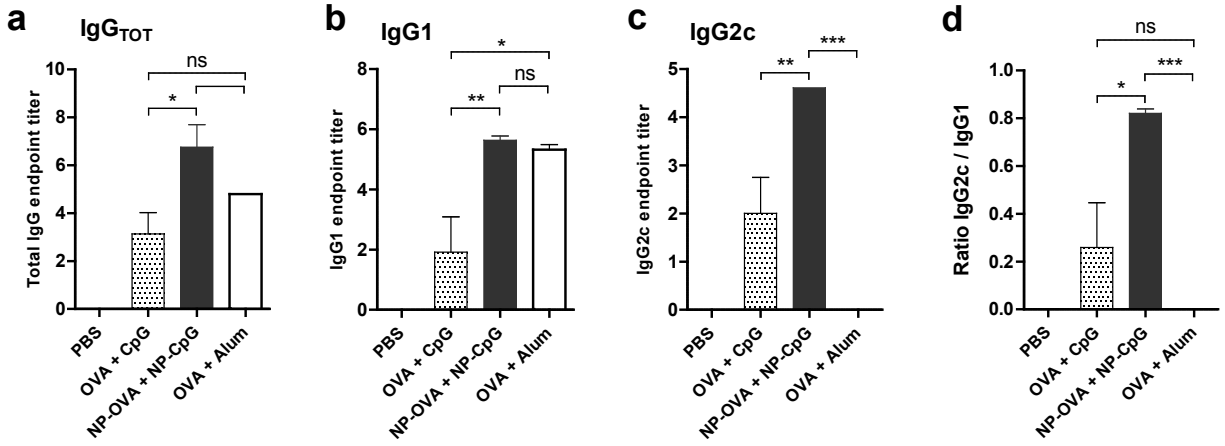


**Figure S9.** Conjugation of OVA and CpG to IONP-filled micelles induces a switch in the immune response to more balanced Th1/Th2 response. 5 µg OVA mixed with 5 µg CpG free or in conjugation with the IONP micelles were injected in C57BL/6 mice on day 0 and 14, subcutaneously in the flanks. OVA-Alum mixture was included for comparison. Mice were sacrificed on day 35 and OVA specific a) total IgG, b) IgG1 and c) IgG2c antibodies are represented. d) Ratio between IgG2c and IgG1 is shown for comparison of Th1/Th2 response to each adjuvant type. Data are presented as mean ± SEM of 5 mice per group. $^{*}P < 0.05$, $^{**}P < 0.01$, $^{***}P < 0.001$, ns = non significant by one-way ANOVA followed by Tukey's test.

The increased ratio between IgG2a and IgG1 antibodies (IgG2a/IgG1 closer to 1) in those mice injected with IONP-OVA micelles indicates a more balanced Th1/Th2 response in the two tested routes, compared to the immunization with OVA free antigen.

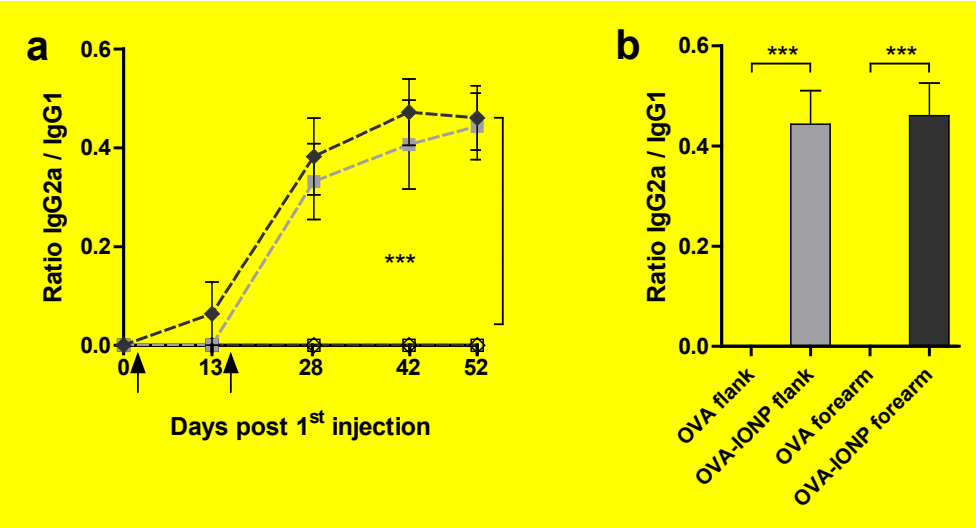


**Figure S9.** Conjugation of OVA to IONP-filled micelles induces a switch in the immune response to more balanced Th1/Th2 response. 5 µg OVA free or in conjugation with the IONP micelles (ca. 25 ng of magnetite) were injected in Balb/c mice on day 0 and 14, subcutaneously in the forearms or in the flanks. Mice were sacrificed on day 52. Anti-OVA IgG2a/IgG1 ratio at a) different time points and b) 52 days after first injection. Data are presented as mean ± SEM of 9 mice per group. ***$P < 0.001$ by a) two-way ANOVA followed by Bonferroni's test and b) one-way ANOVA followed by Tukey's test.

Gating strategy followed for each flow cytometry assay.

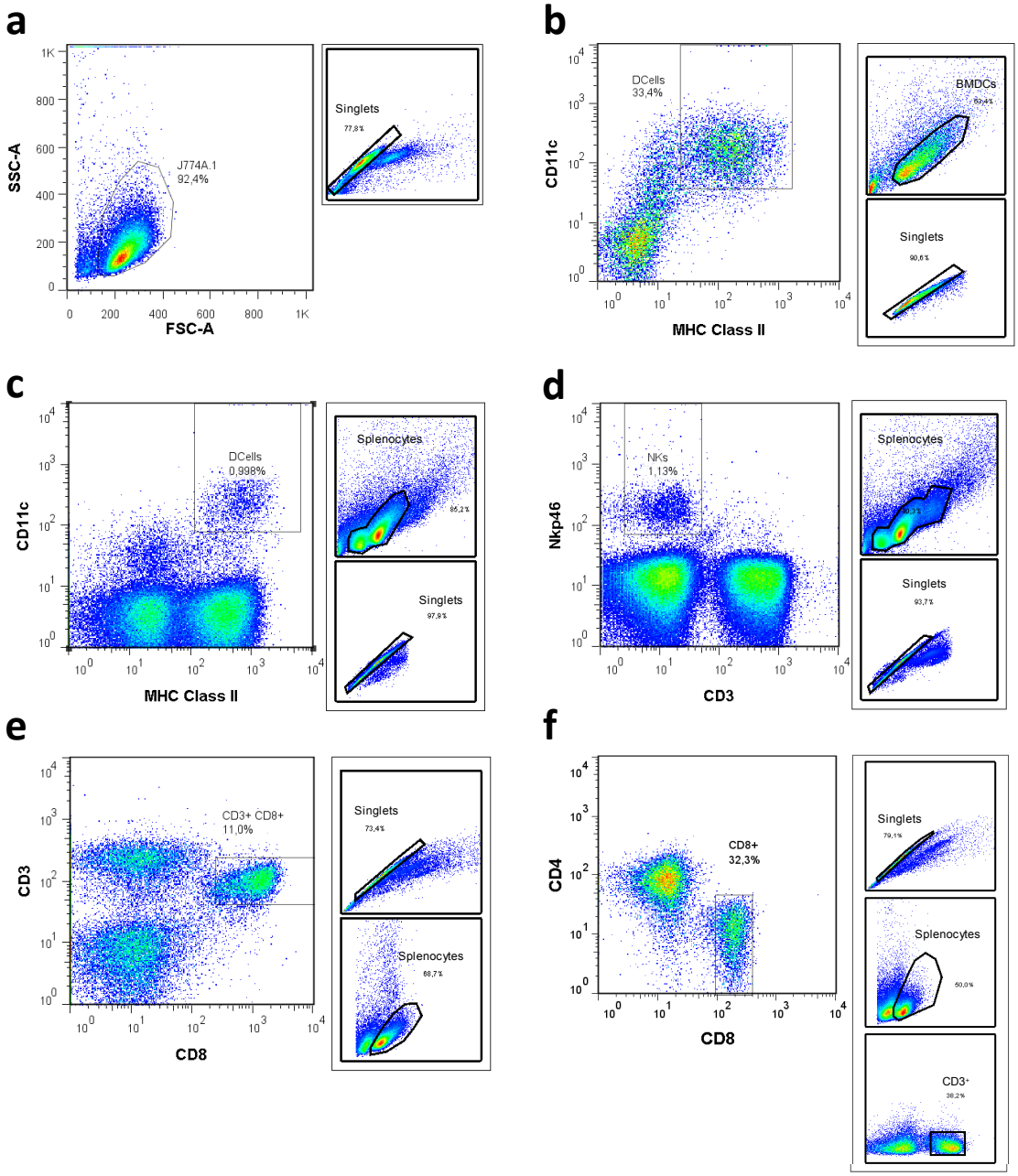


**Figure S10.** Cell gating strategies for the different assays. a) J774A.1 macrophages cell line, for IONP uptake assays; b) DC gating into the bone marrow derived cells (BMDCs), for maturation assays. For the assessment of the innate immune response, c) DC and d) NK cells were gated into the splenocytes. $CD8^+$ T cell gating for both e) SIINFEKL-specific cells and f) intracellular IFN-γ production analysis.